J. Fluid Mech. (2022), *vol*. 944, A41, doi:10.1017/jfm.2022.532

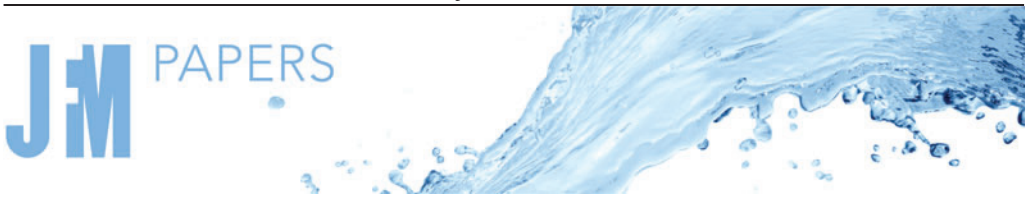

Helicity dynamics in viscous vortex links

Jie Yao[1],†, Weiyu Shen[2], Yue Yang[2] and Fazle Hussain[1]

[1]Department of Mechanical Engineering, Texas Tech University, Lubbock, TX 79409, USA

[2]State Key Laboratory for Turbulence and Complex Systems, College of Engineering, Peking University, Beijing 100871, PR China

(Received 5 October 2021; revised 25 April 2022; accepted 13 June 2022)

The dynamics of two slender Hopf-linked vortex rings at vortex Reynolds numbers ($Re \equiv \Gamma/\nu$, circulation/viscosity) 2000, 3000 and 4000 is studied using direct numerical simulations of the incompressible Navier–Stokes equations. Under self-induction, the initially perpendicularly placed vortex rings approach each other and reconnect to form two separate vortex rings. The leading ring is closely cuddled and further undergoes secondary reconnection to form two even smaller rings. At high Re, the leading ring and the subsequent smaller rings are unstable and break up into turbulent clouds consisting of numerous even smaller-scale structures. Although the global helicity H remains constant before reconnection, it increases and then rapidly decays during reconnection – both the growth and decay rates increase with Re. In the two higher Re (i.e. 3000 and 4000) cases, H further rises after the first reconnection and reaches a quasi-plateau with the asymptotic value continuously increasing with Re – suggesting that H for viscous flows is not conserved at very high Re. Further flow analysis demonstrates that significant numbers of positive and negative helical structures are simultaneously generated before and during reconnection, and their different decay rates is the main reason for the complex evolution of H. By examining the topological aspects of the helicity dynamics, we find that, different from H, the sum of link and writhe ($L_k + W_r$) continuously drop during reconnection. Our results also clearly demonstrate that the twist, which increases with Re, plays a significant role in the helicity dynamics, particularly at high Re.

Key words: vortex dynamics

1. Introduction

According to Noether's theorem, conservation laws and symmetries are at the heart of physics. For a fluid system, in addition to energy, there is another important inviscid invariant: helicity H, which is defined as $H = \int_V h \, \mathrm{d}V$ with V the entire flow volume

† Email address for correspondence: jie.yao@ttu.edu

and $h = \boldsymbol{u} \cdot \boldsymbol{\omega}$ being the helicity density ($\boldsymbol{u}$ and $\boldsymbol{\omega}$ are the velocity and vorticity fields, respectively). Helicity measures the degree to which vortex lines embedded in a fluid system wind around each other (Moreau 1961; Moffatt 1969) and is believed to play an essential role in turbulence cascade and fine-scale mixing. In addition, the importance of helicity is underscored by the growing awareness of the roles of links and knots on various physical systems, e.g. fluids (Kleckner & Irvine 2013), plasmas (Ricca & Moffatt 1992), liquid crystals (Martinez *et al.* 2014) and biology (Chichak *et al.* 2004).

For finite thickness vortex tubes, Moffatt (1969) and Moffatt & Ricca (1992) showed that the helicity could be geometrically decomposed as

$$H = \sum_{i \neq j} \Gamma_i \Gamma_j L_{k,ij} + \sum_i \Gamma_i^2 (T_{w,i} + W_{r,i}), \tag{1.1}$$

where Γ_i is the circulation of vortex tube i, $L_{k,ij}$ is the Gauss linking number between tubes i and j and $W_{r,i}$ and $T_{w,i}$ are, respectively, the writhe and twist of the tube i. Note that both L_k and W_r can be obtained from the vortex tube centreline alone; however, the twist T_w and global helicity H – the former consisting of the torsion twist (T_t) of the axis and the internal intrinsic twist (T_i) of vortex lines within the core – require additional measurements inside each vortex tube.

The conservation of helicity in ideal (inviscid) fluids is a direct consequence of the Helmholtz laws of vortex motion. As the conservation laws are fundamental to flow dynamics, whether the conservation of helicity can be extended to viscous flows at very high Reynolds number (Re) is a significant question. In viscous flows, vorticity diffuses, allowing nearby vortex tubes to reconnect (Kida & Takaoka 1994; Yao & Hussain 2022). There have been extensive debates regarding helicity evolution in viscous fluids, including the extent of its conservation and potential mechanisms for its transfer between different forms (i.e. link, writhe and twist) (Kleckner & Irvine 2013). On the one hand, viscosity can alter the field-line topology during the reconnection process – breaking the conservation of helicity. On the other hand, as helicity dissipation occurs at small scales, one may argue that, for a slender vortex (i.e. when the core size is much smaller than the radius of curvature), the localized viscous effect near the reconnection region would not significantly alter the global helicity at sufficiently high Re, which mainly resides in large scales (Kivotides & Leonard 2021).

Given its importance, numerous research studies in the past decades have addressed the helicity dynamics in real fluids. For example, Kida & Takaoka (1987, 1988) conducted the direct numerical simulation (DNS) of a trefoil knotted vortex and observed that H slowly decreases during the whole evolution. They further found that the decay rate decreases with increasing Re, which seems to imply that H is conserved at a sufficiently high Re. Two vortex rings in the Hopf link configuration have also been studied using DNS by Aref & Zawadzki (1991) and Kivotides & Leonard (2003). Note that all these earlier studies were performed at relatively low Re, where viscous effects (i.e. diffusion and dissipation) are relatively strong. Irvine and co-workers (Kleckner & Irvine 2013; Scheeler *et al.* 2014) experimentally created vortex links and knots in a water tank at relatively high $Re(\sim 2 \times 10^4)$ and observed that the centreline helicity (i.e. sum of link and writhe helicities) is conserved during the topological change. Note that their experimental techniques did not allow them to directly measure the twist, and all their claims are drawn based on the link/writhe calculated from the tracked vortex centrelines and the assumption of a negligible effect of twist due to rapid viscous dissipation. Inspired by the studies of Irvine and co-workers, Kerr (2018*b*) numerically studied the evolution of a perturbed trefoil knotted vortex and confirmed that the helicity is conserved before reconnection,

followed by a progressive decay after reconnection. Recently, Kivotides & Leonard (2021) employed reconnection-capable vortex filament methods to investigate the topological and helicity dynamics of vortex links for moderate and high Re. By discretizing the finite-core vortex tubes into bundles of a finite number of filaments, they demonstrated that the helicity of linked vortex rings is conserved during the unlinking process, and most of the initial link converts to writhe during the post-reconnection evolution. Note that the vortex filament simulation by Kivotides & Leonard (2021) did not take into account contributions from the intrinsic twist T_i to the total helicity. They also performed a DNS of vortex link at $Re = 1500$ using the finite-volume method and found that the helicity continuously decreases, which, similar to that observed by Kida & Takaoka (1987), is attributed to strong viscous dissipation at low Re. Recently, Zhao *et al.* (2021) conducted DNS of a trefoil knotted vortex for $Re \leq 6000$ using the adaptive mesh refinement technique and found that H experiences a sudden jump during reconnection at high Re. Yao, Yang & Hussain (2021) performed DNS of a trefoil knotted vortex constructed using the method developed by Xiong & Yang (2019, 2020*a*) for Re up to 12 000 and also observed that H grows during and after reconnection with the rate of growth increasing with Re. They further showed that the increase of H is mainly attributed to the generation of twist (include both positive and negative signs) before and during reconnection, which contrasts with the previous claims that the twist has a negligible effect on the helicity dynamics.

In addition to the above-mentioned works for classical fluids, there are also studies of linked or knotted vortex in quantum fluids. For example, Scheeler *et al.* (2014) simulated the evolution of trefoil knots in a superfluid with the Gross–Pitaevskii equation and observed that the centreline helicity experiences a discrete jump across the reconnection. Zuccher & Ricca (2017) analysed the evolution of linked vortex rings, which, through multiple reconnections, cascade into three unlinked and almost planar vortex loops. They further found that the total helicity remains unchanged throughout the process, and the link helicity is gradually transferred to writhe and (torsion) twist helicities, followed by a continuous relaxation of twist across scales.

The objective of this work is to investigate the helicity and topological dynamics of vortex links in viscous flows. In particular, we aim to address whether helicity is conserved during the unlinking process. The rest of the paper is organized as follows. The details of the initial configuration and numerical set-up are given in § 2. The overall flow evolution and statistics are presented in § 3. The detailed helicity and the topological dynamics are discussed in §§ 4 and 5, respectively. Finally, conclusions are drawn in § 6.

2. Initial configuration and numerical set-up

The initial condition (figure 1) consists of two vortex rings in the Hopf-link configuration (i.e. $\alpha = 90^\circ$). The radius of the ring is selected as $R_0 = 1$. The initial vorticity distribution in the cross-section of the ring is assumed to be Gaussian along the radial direction

$$\omega(\rho) = \frac{\Gamma_0}{2\pi\sigma^2} \exp\left(-\frac{\rho^2}{2\sigma^2}\right), \tag{2.1}$$

where the circulation $\Gamma_0 = 1$, and the standard deviation $\sigma = 1/(16\sqrt{2\pi}) \approx 0.025$. The effective core radius is estimated as $r_e = 2\sigma$, within which the vortex tube contains 95 % of the circulation; hence, the ratio between the mean radius and core size $R_0/r_e = 8\sqrt{2\pi} \approx 20$. In the current study, the vorticity direction of two rings are chosen so that they have the same chirality; hence, the total Gauss linking number $L_k = \sum_{ij} L_{k,ij} = 2$. The two rings lie in planes whose normal vectors are inclined at 45° to the z-axis. In this way, the total

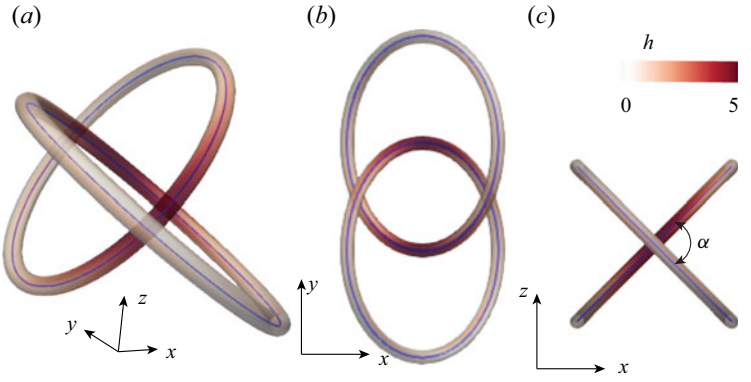

Figure 1. (*a*) Oblique, (*b*) top and (*c*) front views of the initial configuration of the Hopf link (represented by vorticity isosurface at 4 % of the maximum initial vorticity colour coded by the helicity density h). Note that $\alpha = 90^\circ$, and the blue lines inside the vortex rings denote the vortex axis.

moment of vorticity defined as

$$\boldsymbol{I} \equiv \frac{1}{2}\iiint_{\mathbb{R}^3} \boldsymbol{x} \times \boldsymbol{\omega}(\boldsymbol{x})\,\mathrm{d}V, \tag{2.2}$$

is non-zero only for the third component. Consequently, the initial two vortex rings and the subsequent rings formed after reconnection have skew symmetry in the x–y plane (e.g. $\omega_z(x, y, z) = \omega_z(-x, -y, z)$) and mainly propagate along the z–direction. If the sign of vorticity in one of the rings is reversed (i.e. the two rings have opposite chiralities), then the link helicity becomes -2, and the moment of vorticity $\boldsymbol{I}$ is non-zero along the x-direction. As the initial writhe W_r and twist T_w of the rings are both zero, the flow evolution is overall the same between these two cases but with a reversed sign of H. Note that as demonstrated in Xiong & Yang (2020*b*), such relationship, in general, is not valid when the initial W_r and T_w are non-zero (e.g. for coiled vortex rings).

DNS of the incompressible Navier–Stokes equations is carried out in a periodic domain $[-\pi : \pi]^3$ using a Fourier pseudospectral algorithm in the velocity–vorticity form (Pradeep & Hussain 2004; Yao & Hussain 2020*a*). Time integration is carried out with an explicit third-order Runge–Kutta scheme, while the viscous term is treated exactly with the integrating factor technique (Canuto *et al.* 2012). Time is non-dimensionalized as $t^* = t/(R_0^2/\Gamma)$. In the current study, we consider three different vortex Reynolds numbers (varied by changing the viscosity ν) $Re = 2000$, 3000 and 4000, with grid points $N^3 = 768^3$, 1280^3 and 1536^3, correspondingly. Grid and domain size convergence analyses are conducted in Appendix A, which clearly demonstrates that both the domain size and the grid resolutions employed here are adequate to capture the flow details.

3. Flow statistics and evolution

3.1. *Flow structures*

Figure 2 (and supplementary movie 1) shows the time progression of flow structures visualized using vorticity magnitude isosurface $|\boldsymbol{\omega}| = 0.04\omega_0$, with ω_0 being the maximum vorticity magnitude at $t^* = 0$. By self-induction, the initially perpendicularly placed vortex rings approach each other and also deform so that the neighbouring parts become anti-parallel and collide with each other. Then, the vortex rings start to reconnect

and untie. Note that two reconnections occur simultaneously due to symmetry. Similar to what is observed for the trefoil knotted vortex (Yao *et al.* 2021), the reconnected parts (called bridges) combine with other parts – forming two separate vortex rings, i.e. a leading ring (LR) and a trailing ring (TR). The coiled TR continues to rotate counter-clockwise as it propagates along the z-direction. On the other hand, the LR is closely cuddled – different from what is observed for the trefoil knotted vortex (Yao *et al.* 2021; Zhao & Scalo 2021). In addition, it continuously decays due to viscous cross-annihilation – similar to that observed by Aref & Zawadzki (1991). Simultaneously, LR further undergoes reconnection to form two smaller rings – akin to that happening for an elliptical vortex ring with a large aspect ratio (Dhanak & Bernardinis 1981; Cheng, Lou & Lim 2016). However, as the LR is strongly polarized (i.e. with strong axial flow), the reconnection here occurs in a much more complex manner, particularly at higher Re. The LR and the subsequent two smaller rings are very unstable due to the presence of strong axial flows and break up to form turbulent clouds consisting of numerous small-scale structures, which then rapidly decay. This is quite different from what was observed by Zuccher & Ricca (2017) for quantum vortex links, where two distinct small rings develop. In addition, due to intense vortex stretching and weak viscous dissipation at high Re, more small scales are generated and wrapped around the TR – similar to what is observed for the trefoil knotted vortex (Yao *et al.* 2021). After $t^* = 10$, as the LR becomes very weak, the flow is mainly dominated by the TR.

Another feature of interest is that, while the vortex rings initially have predominately positive helicity density (i.e. $+h$), some segments acquire negative helicity (i.e. $-h$) before and during reconnection, particularly at the tips of the rings. These $-h$ structures become more prominent and persist longer in time at higher Re. Hence, different from the previous well-studied scenario, where the two vortices undergoing reconnection are symmetrical, the reconnection here is asymmetric – similar to that considered by McGavin & Pontin (2019) and Yao *et al.* (2021) for anti-parallel vortex reconnection with axial flows. Such asymmetric reconnection is also observed during the reconnection of a trefoil knotted vortex (Yao *et al.* 2021; Zhao *et al.* 2021) and is the main reason for helicity increase during reconnection (Zhao & Scalo 2021). In addition, the $+h/-h$ zones appear alternatively in the TR at a late time (e.g. $t^* = 10$ in figure 2*c*), which implies the presence of strong oscillations of axial flow/twist.

3.2. *Flow statistics*

Figures 3(*a*) and 3(*b*) show the time evolution of energy $E = \int_V (\boldsymbol{u}^2/2)\,\mathrm{d}V$ and enstrophy $\Omega = \int_V (\boldsymbol{\omega}^2/2)\,\mathrm{d}V$ for three different Re cases. The energy E monotonically decays, and the decay rate depends on viscosity and enstrophy, namely $\mathrm{d}E/\mathrm{d}t = -2\nu\Omega$. As a result, the decay of E is enhanced during reconnection due to increased enstrophy. The enstrophy initially decays due to viscous dissipation, and the decay rate decreases with increasing Re due to the limited viscous effect. For a rectilinear Lamb–Oseen vortex, the rate of change of enstrophy is $(1/\Omega)\partial\Omega/\partial t = 2\nu/\sigma^2$ with the core size σ growing as $\sigma(t) = \sqrt{\sigma_0^2 + 2\nu t}$ (Yao *et al.* 2021). Consequently, the enstrophy should follow $\Omega(t) = \Omega_0 \exp[-\int_0^t (2\nu/\sigma^2]\,\mathrm{d}t$ with Ω_0 being the enstrophy at $t^* = 0$. For the linked vortices considered here, the initial decrease of Ω also agrees with this prediction, but the agreement deteriorates as Re increases – probably due to enhanced enstrophy production caused by vortex stretching. When reconnection starts, Ω experiences rapid growth due to the generation of numerous small scales, and the peak of Ω increases with Re – akin to what was found by Yao & Hussain (2020*b*). In addition, with increasing Re,

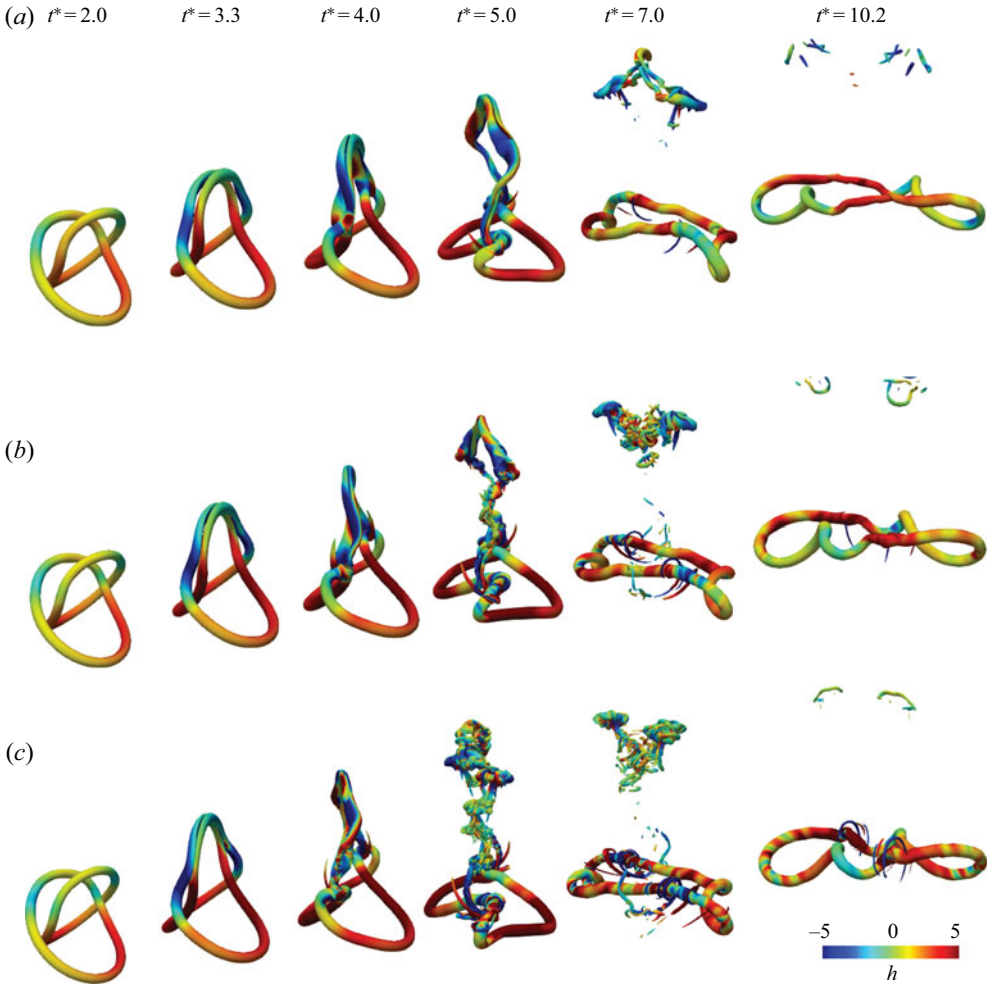

Figure 2. Evolution of flow structures represented by vorticity isosurface at 4 % of maximum initial vorticity ($|\boldsymbol{\omega}| = 0.04\omega_0$) shaded with helicity density $h = \boldsymbol{u} \cdot \boldsymbol{\omega}$ for (*a*) $Re = 2000$, (*b*) $Re = 3000$ and (*c*) $Re = 4000$. See also supplementary movie 1 available at https://doi.org/10.1017/jfm.2022.532 for the time evolution of different *Re* cases.

the time for Ω to reach the peak value slightly decreases – suggesting that the reconnection happens earlier at higher *Re*. It is somehow expected as the self-induced velocity of the vortex ring increases at higher *Re* – due to smaller core size as the viscous diffusion is suppressed (Saffman 1970). Also, the duration of the increase of Ω is shorter, implying that reconnection is more rapid at higher *Re*. Such a *Re*-trend has also been observed by Zhao *et al.* (2021) and Yao *et al.* (2021) for a trefoil knotted vortex. The enstrophy then again experiences an exponential drop after the peak – the drop rate increasing with *Re* this time, because more numerous and smaller scales are generated at higher *Re* during reconnection.

The evolution of the global helicity H (figure 3*c*) is more interesting and complex. Initially, H remains almost constant – equal to the link helicity $\Gamma^2 L_k$ (i.e. $= 2$). It rapidly grows when reconnection starts, followed by a rapid drop. And the rates of growth/drop increase with *Re*. Note that such a rapid decay of H is not observed for the trefoil knotted

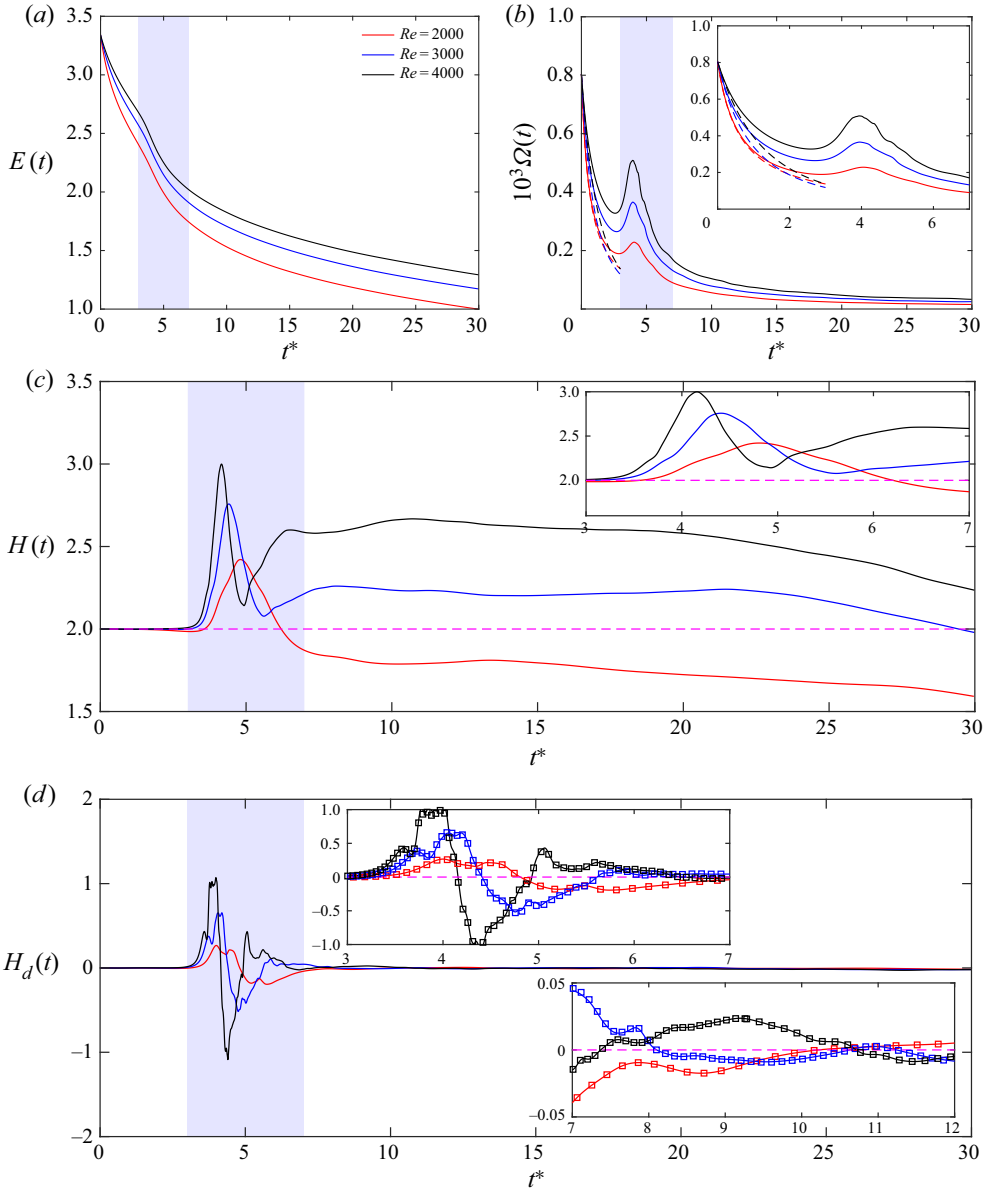

Figure 3. Time evolution of (*a*) energy E, (*b*) enstrophy Ω, (*c*) global helicity H and (*d*) helicity dissipation H_d for $Re = 2000$ (red), 3000 (blue) and 4000 (black). Note that the shaded regions represent the time intervals when reconnection is happening. The dashed lines in (*b*) denotes $\Omega(t) = \Omega_0 \exp[-\int_0^t (2\nu/\sigma^2]\mathrm{d}t$ with $\sigma = \sqrt{\sigma_0^2 + 2\nu t}$. The dashed line in (*c*) denotes the initial value of helicity; and the square symbols in (*d*) correspond to the time derivative of H (the left-hand side of (3.1)).

vortex case (Yao *et al.* 2021). As will be shown later, it is mainly due to the evolution of the LR. In addition, the peak value of H also increases with Re, namely, from $H = 2.42$ at $Re = 2000$ to 3.0 at $Re = 4000$. Although the peak of H occurs earlier as Re increases, which is again consistent with the earlier reconnection at higher Re. Despite the fact that H eventually decays at late times (e.g. $t^* > 20$), its evolution immediately after reconnection

strongly depends on Re. While H slowly decays at $Re = 2000$, it increases before reaching a quasi-steady state at high Re, and the growth becomes more rapid at higher Re. From this Re trend, it is clear that H would continuously increase at even higher Re. This indicates, in conjugation with the previous findings by Zhao *et al.* (2021) and Yao *et al.* (2021) for the trefoil knotted vortex, that H is not conserved during the unlinking/untying process, which contradicts the claims made by Scheeler *et al.* (2014) and Kivotides & Leonard (2021) that the helicity is conserved for $Re \to \infty$. The oscillation of $H(t)$ during and after reconnection is quite surprising and is mainly attributed to the LR formed during reconnection. To confirm this, we consider the evolution of vortex link with a smaller angle (i.e. $\alpha = 30^\circ$) in Appendix B. Similar to reconnection of a trefoil knot vortex, two distinct rings form after reconnection for this case. In addition, the strong oscillation of H (i.e. rapid increase/decrease) is not observed there – suggesting that the evolution of H after reconnection strongly depends on the initial configurations.

The governing equation for the global helicity H is

$$\frac{\mathrm{D}H}{\mathrm{D}t} = \underbrace{-\iiint 2\nu\boldsymbol{\omega}\cdot(\boldsymbol{\nabla}\times\boldsymbol{\omega})\,\mathrm{d}V}_{H_d}, \tag{3.1}$$

where the right-hand side is viscous dissipation H_d with $\boldsymbol{\omega}\cdot(\boldsymbol{\nabla}\times\boldsymbol{\omega})$ being the so-called 'superhelicity' (Brissaud *et al.* 1973; Hide 1989; Scheeler *et al.* 2014). As H is not positive-sign definite, H_d can be either positive or negative – quite different from energy or enstrophy dissipation. The negative/positive values of H_d represent decreases/increases of H, respectively. Therefore, H_d can either be a source or sink of H. Nevertheless, as will be shown later, the helicity dissipation density $h_d(\equiv -2\nu\boldsymbol{\omega}\cdot(\boldsymbol{\nabla}\times\boldsymbol{\omega}))$, in general, is negative/positive where h is positive/negative, respectively. For a twisted rectilinear vortex column (i.e. Batchelor vortex), the relative dissipation of helicity (in the form of twist) depends mainly on core size σ and viscosity ν, i.e. $H_d/H = -2\nu/\sigma^2$; and, therefore, helicity is expected to decay exponentially $H(t)/H(0) = \exp[-\int_0^t (2\nu/\sigma^2)\,\mathrm{d}t]$ (Scheeler *et al.* 2014; Yao *et al.* 2021).

Figure 3(*d*) shows the evolution of H_d for three different Re. It remains almost zero for $t^* < 3$, becomes positive as reconnection starts and continuously increases and reaches the peak almost at the same time as the enstrophy (figure 3*b*). In addition, as Re increases, the growth of H_d starts earlier and at a larger rate – again due to an earlier and faster reconnection at higher Re. As the reconnection slows down, H_d decreases and becomes even negative. And with increasing Re, the minimum value of H_d becomes smaller and occurs at an earlier time. Then, H_d non-monotonically increases with time and becomes positive again. At the very late time (i.e. $t^* > 15$), H_d becomes very small – consistent with the slow decay of H observed in figure 3(*c*). As substantial variations of H_d, as well as of H, mainly occur during and immediately after reconnection (i.e. $t^* < 12$), in the following section, we will mainly examine their evolution during this period.

To further shed light on the helicity evolution, figure 4 shows the time evolution of helicity integrated in the x–y plane, defined as

$$\langle h\rangle(z,t) = \iint h\,\mathrm{d}x\,\mathrm{d}y. \tag{3.2}$$

The evolution of $\langle h\rangle$ is overall quite similar at different Re, except that the amplitude is larger at higher Re. At $t^* = 0$, $\langle h\rangle$ is non-zero (positive) only in a narrow range of z, where the two vortex rings initially reside (i.e. $-3 < z < -1.5$). As time progress, the positive patch (i.e. $+\langle h\rangle$) advects towards larger z values as the two rings move upwards.

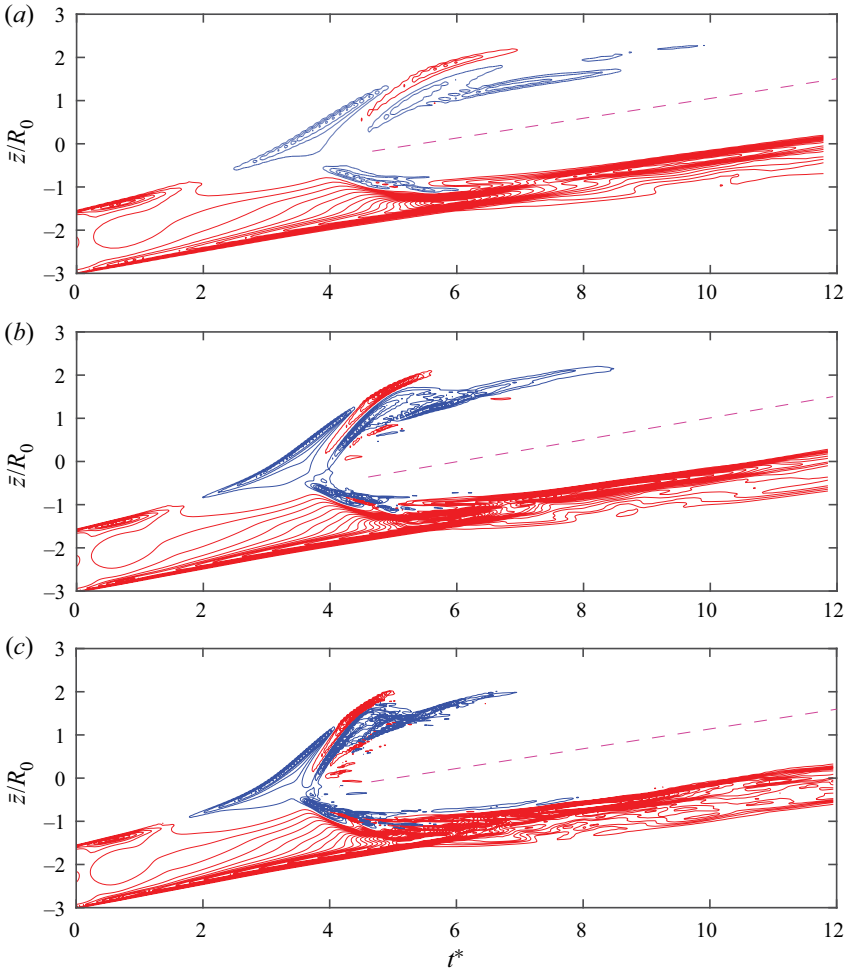

Figure 4. Time evolution of x–y plane-integrated helicity $\langle h\rangle(z, t)$ for (*a*) $Re = 2000$, (*b*) 3000 and (*c*) 4000. Positive and negative isocontours $[0.25 : 0.25 : 20]$ of initial maximum $\langle h\rangle$ (i.e. $\max(\langle h\rangle(z, 0))$) are shown in red and blue, respectively.

Interestingly, around $t^* = 2$, $-\langle h\rangle$ develops at large z, further increasing at later times. This is consistent with figure 2 showing that the top parts of the rings are predominantly associated with negative helicity density (i.e. $-h$). Then, as the two new vortex rings form and separate after reconnection, $\langle h\rangle$ splits into two parts. Although there are some $-\langle h\rangle$ patches at the top of the trailing part (i.e. TR), it expeditiously disappears. In addition, the TR carries the majority of H, particularly at late times. For the leading part (i.e. LR), $\langle h\rangle$ is initially all negative, suggesting that the LR, in contrast to the TR, has dominantly $-h$. Interestingly, a narrow band of $+\langle h\rangle$ develops in LR, and then is rapidly replaced by strong $-\langle h\rangle$, which also diminishes at a late time.

4. Helicity dynamics

4.1. *Pre-reconnection*

Before reconnection ($t^* \leq 3$), H remains almost constant. However, it does not mean that there is no generation of h during this period. Instead, due to the helicity splitting

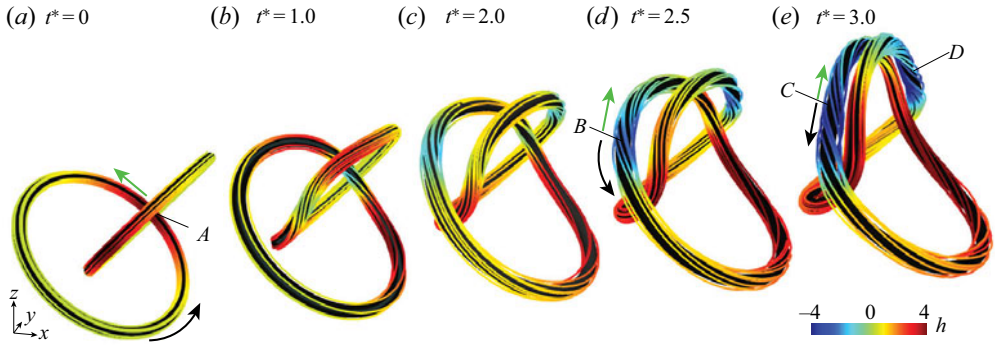

Figure 5. Earlier evolution ($0 \leq t^* \leq 3$) of flow structures represented by vortex lines shaded with helicity density $h = \boldsymbol{u} \cdot \boldsymbol{\omega}$ for $Re = 3000$. The black and green arrows indicate the directions of vorticity and axial velocity, respectively.

mechanism discussed in Yao & Hussain (2021), $\pm h$ are simultaneously developed. To demonstrate this, figure 5 shows the early time evolution (i.e. $t^* \leq 3$) of flow structures represented by the vortex lines colour coded by h. For the linked vortex rings, the mutual interaction is one of the main contributors to h. Initially, h is positive everywhere, attaining its maximum near the centre of the vortex rings (i.e. A in figure 5a), where the induced velocity by the other ring is the largest and aligns with the vorticity. The two rings deform as they move close to each other due to self-induction. At the top parts, the two rings become anti-parallel and rapidly move upward as a dipole due to mutual induction. Consequently, at region B in figure 5(d), the velocity is directed opposite to that of vorticity – resulting in the development of $-h$. As the rings move closer to each other, the higher mutual induction causes a much stronger $-h$ (regions C and D in figure 5e). As explained later, the h generated due to mutual induction is mostly at large scales and associated with the link and writhe helicities.

In addition to mutual induction, there is another important mechanism of helicity density generation; namely, the twist of vortex lines with respect to the vortex centreline. Initially, all the vortex lines aligned with the vortex rings (figure 5a). As the rings evolve, the vortex lines become twisted, which, as discussed by Melander & Hussain (1994), is mainly due to the vortex core dynamics. This process can be better illustrated by considering a simplified model – interaction between a vortex ring and a rectilinear tube (figure 6a), which is a good approximation of what occurs around region A in figure 5(a). Due to the variation of the induced velocity of the vortex ring, the vortex tube is compressed (i.e. $\omega_z \partial w/\partial z < 0$) and stretched (i.e. $\omega_z \partial w/\partial z > 0$) above and below the ring, respectively – resulting in a variation of the core size along the tube. As the vorticity magnitude is higher/lower in the region with a small/large core size, the initially straight vortex lines become radially displaced and undergo coiling (Melander & Hussain 1994; Yao & Hussain 2021). Note that the vortex lines are oppositely twisted with respect to planes A and B; hence both $+h$ and $-h$ are generated simultaneously. Furthermore, as the vortex tube is, respectively, compressed and stretched above and below the ring, the twist of the vortex lines is correspondingly enhanced and suppressed. This explains the twists of vortex lines observed at regions C and D in figure 5(e) – particularly why the vortex lines in one segment are more twisted than in the other. Note that the h generated through the twist of vortex lines is at small scales and is mainly associated with the twist helicity.

The generation of $\pm h$ increases with increasing Re. To confirm that, following Yao *et al.* (2021), figure 6(b) shows the volume integrated positive and negative helicity

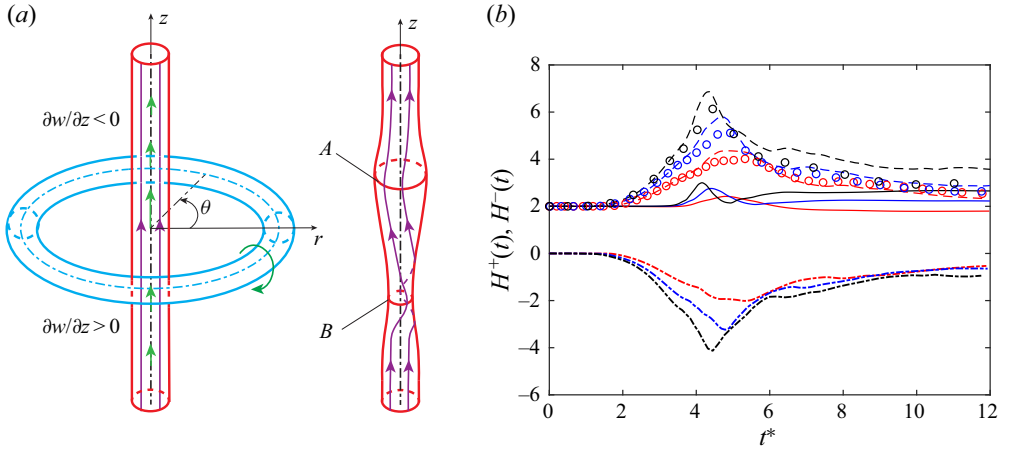

Figure 6. (*a*) Schematic of helicity density generation through the coiling of vortex lines; and (*b*) time evolution of H^+ (dashed) and H^- (dash-dotted) for $Re = 2000$ (red), 3000 (blue) and 4000 (black). Note that the solid lines in (*b*) represent the global helicity, and the circles denote $-H^-(t) + H(0)$ with $H(0) = 2$ the initial global helicity.

$H^\pm = \int h^\pm \, \mathrm{d}V$, where

$$h^+ = \begin{cases} h, & \text{if } h \geq 0 \\ 0, & \text{otherwise} \end{cases}, \tag{4.1}$$

and $h^- = h - h^+$. As expected, $H^+(0) = H(0)$, and $H^-(0)$ is zero at $t^* = 0$. Both the H^- and H^+ slowly grow in magnitude during the initial approach stage, when the two vortex rings form anti-parallel structures. Just before reconnection, both of them rapidly increase – at roughly the same rate; hence, H remains constant. In addition, the growth rate of $|H^\pm|$ increases with Re. During reconnection, although the magnitudes of H^- and H^+ still increase, but with different rates. By comparing H^+ and $H^- + H(0)$, it is clear that H^+ grows faster – resulting in an increase of H. Then, the magnitudes of both H^+ and H^- decrease, but with a different decay rate – akin to that observed by Yao *et al.* (2021) for a trefoil knotted vortex.

Several comments deserve to be made here. First, as both the two helicity generation mechanisms discussed above are purely inviscid, they would also occur for Euler flows – despite the fact that reconnection would be strictly prohibited. Second, the evolution of vortex lines, particularly their strong twists, is quite different from that observed by Kivotides & Leonard (2021), who used a bundle of a finite number of filaments to represent finite-core vortex rings. Due to the inability to capture the detailed core dynamics, one should be very cautious about using the vortex filament method for understanding the helicity dynamics in viscous flows. Finally, the rapid generation of $\pm h$ and their decays are essential prerequisites for the oscillation of H observed during and after reconnection. As shown later, the difference in the growth and decay rates of H^+ and H^- is the main reason for the increase or decrease of H observed in figure 3(*c*).

4.2. *During reconnection*

As discussed in § 3.2, H rapidly rises during reconnection, particularly at high Re. Such an increase has also been observed during the unknotting process of a trefoil knotted vortex (Yao *et al.* 2021; Zhao *et al.* 2021). For both of these configurations, $\pm h$ patches are

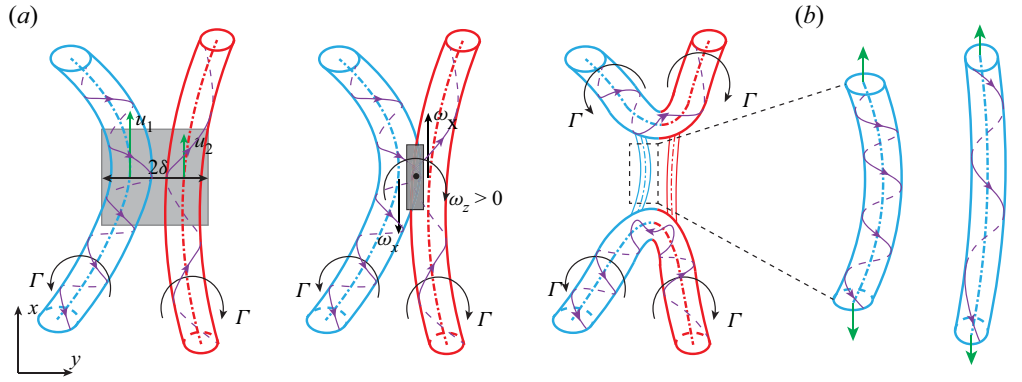

Figure 7. (*a*) Schematic of the helicity dissipation during asymmetric reconnection of two anti-parallel vortex segments with different axial flows; and (*b*) the thread details.

developed in the anti-parallel vortex structures before reconnection due to the helicity density generation mechanisms discussed above. In addition, due to the asymmetry presented in these two anti-parallel segments, the one with $-h$ is much stronger (as shown in figure 5(*e*) and further sketched in figure 7*a*). During reconnection, both $+h$ and $-h$ patches are then expected to be annihilated through viscous dissipation, and the more rapid dissipation of $-h$, presumably due to the larger amplitude, causes the net increase of H.

Recently, Zhao & Scalo (2021) provided an analytical expression relating helicity dissipation to circulation transfer, i.e.

$$\frac{\mathrm{D}H}{\mathrm{D}t} = -2(u_1 - u_2)\delta\frac{\mathrm{d}\Gamma}{\mathrm{d}t}. \tag{4.2}$$

Here, u_i is the axial velocity in the ith vortex segment, δ and $\mathrm{d}\Gamma/\mathrm{d}t$ are the characteristic length scale of the reconnection region and circulation transfer rate between the two segments. Equation (4.2) suggests that, when the axial flows in the two interacting vortices have the same strength, H will remain unchanged during reconnection – consistent with what was observed by Yao & Hussain (2021) for the symmetrical collision of two vortex rings. Once there is a difference between axial flows within the two interacting vortices, H would change during reconnection. This point is further demonstrated in Appendix C by considering the asymmetric collision of two slender vortex rings. In addition, the rate of change of H is proportional to the circulation transfer rate (i.e. $\mathrm{d}\Gamma/\mathrm{d}t$) and the difference in axial velocity (i.e. $u_1 - u_2$) – agreeing with the more rapid increase of H at higher Re (figure 3*d*). This can also be explained by considering the sketch in figure 7(*a*). The difference between the axial velocities in the two vortex tubes results in a non-zero ω_z, which, together with the vorticity gradient $\partial\omega_x/\partial y$, yields positive helicity dissipation h_d – predominant $-\nu\omega_z\partial\omega_x/\partial y$. Furthermore, h_d increase at higher Re due to the much stronger vorticity gradient $\partial\omega_x/\partial y$ (Yao & Hussain 2020*b*). Zhao & Scalo (2021) demonstrated that, at low Re, (4.2) can successfully connect the change of H with the reconnection process, and that, at high Re, the correlation between helicity changes and circulation transfer decreases due to the complex nature of reconnection (Kerr 2018*a*; Yao & Hussain 2020*b*, 2021).

To elaborate on the discussion above, figure 8 shows the evolution of flow structures represented by vortex lines colour coded by h for $Re = 3000$ during reconnection.

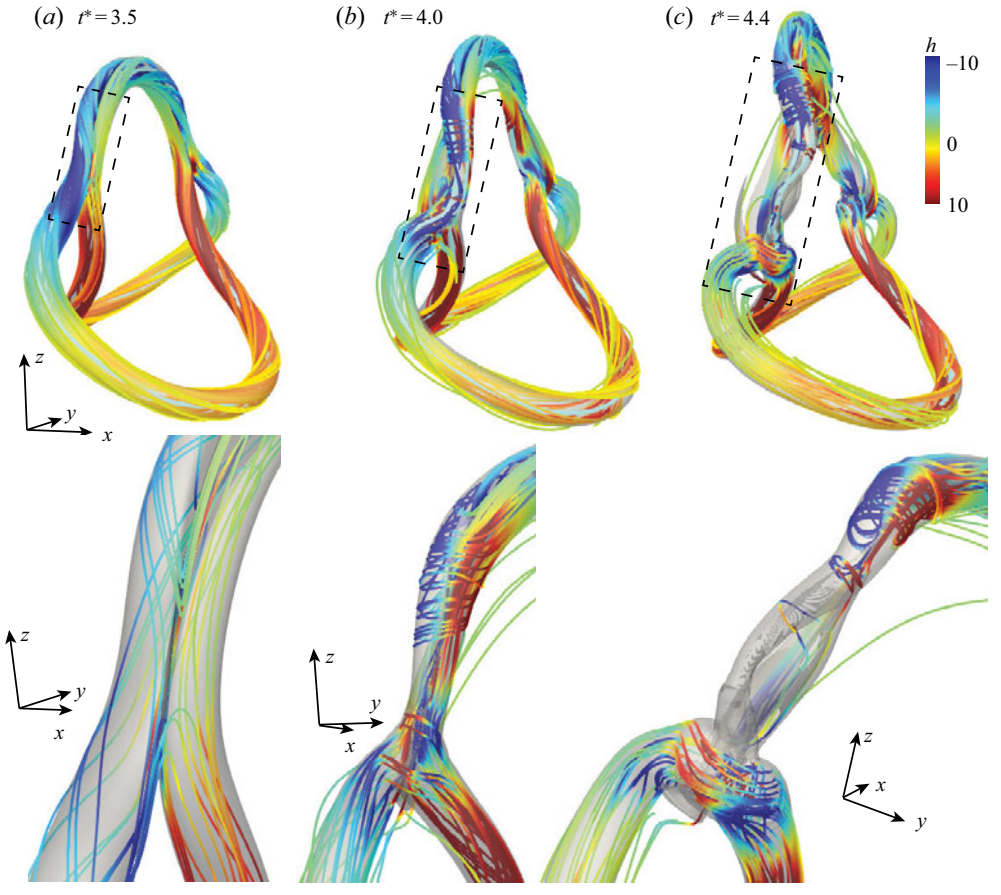

Figure 8. Evolution of flow structures represented by vortex lines shaded with helicity density $h = \boldsymbol{u} \cdot \boldsymbol{\omega}$ for $Re = 3000$ during reconnection: (*a*) $t^* = 3.52$, (*b*) $t^* = 4.04$ and (*c*) $t^* = 4.37$. Note that the bottom row shows the corresponding zoomed-in view of the reconnection region.

The vortex lines in the left ring are more twisted – consistent with the fact that the magnitude of h is larger. As the two vortex rings closely touch, the vortex lines near the periphery start to cut and connect. The reconnected vortex lines form cusps and rapidly recede away from the reconnection site by their sharp curvature-driven self-induction – similar to that observed for symmetrical anti-parallel vortex reconnection (Melander & Hussain 1988; Kida & Takaoka 1994). Successive reconnected vortex lines are similarly laid on top of each other and combine to form progressively stronger bridges. As in reconnection of anti-parallel vortex tubes with axial flows, the two bridges are not symmetric. In addition, due to compression, the reconnection vortex lines in the top bridge are so close that they can reconnect among themselves to form new loops. Furthermore, the induced velocity of the bridges continuously stretches the unreconnected threads, straightening the initially kinked and twisted vortex lines (as sketched in figure 7*b*) and causing the loss of h there (mainly in the form of twist). Since structures in this region are predominantly associated with $-h$ before reconnection, their more rapid decrease during reconnection yields an overall increase of H.

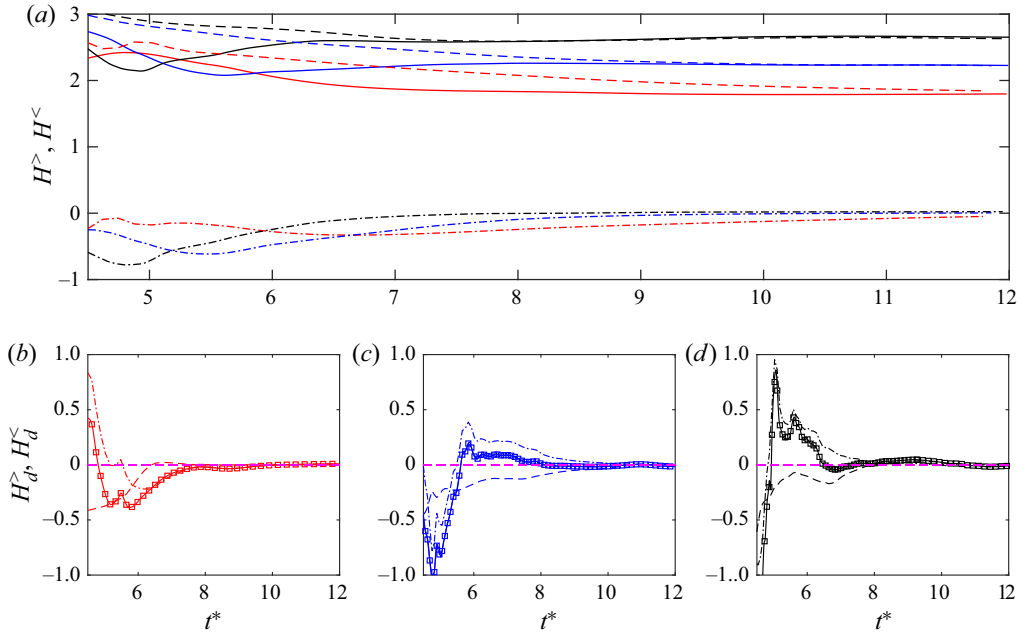

Figure 9. (*a*) The helicity for the top LR $H^>$ (dash-dotted) and bottom TR $H^<(t)$ (dashed) at different *Re*; and the corresponding helicity dissipation $H_d^>(t)$ (dash-dotted) and $H_d^>(t)$ (dash) for (*b*) $Re = 2000$, (*c*) $Re = 3000$ and (*d*) $Re = 4000$. Note that, in (*a*), the solid lines represent the global helicity H; and in (*b–d*), the solid lines denote the global helicity dissipation H_d, and the square symbols correspond to the time derivative of H (the left-hand side of (3.1)).

4.3. *Post-reconnection*

The evolution of H after reconnection is complicated and can be better explained by examining the LR and TR, separately. Figure 9(*a*) shows the helicity for the top $H^>(t)$ (i.e. LR) and bottom $H^<(t)$ (i.e. TR) parts, defined as

$$H^>(t) = \int_{z_s}^{\pi} \langle h \rangle \, \mathrm{d}z, \quad H^<(t) = \int_{-\pi}^{z_s} \langle h \rangle \, \mathrm{d}z, \tag{4.3a,b}$$

where z_s represents the separation location between the LR and TR (denoted by the dashed lines in figure 4). In addition, figure 9(*b–d*) shows the corresponding helicity dissipation $H_d^>(t)$ and $H_d^>(t)$ for $Re = 2000$, 3000 and 4000, respectively.

As the TR predominately has positive h, $H^<$ is positive. At low *Re* (i.e. 2000), it continuously decreases with time, and the corresponding $H_d^<$ remains negative for all times. Due to increased generation of h before and during reconnection, the magnitude of $H^<$ grows with *Re*. In addition, the decay rate of $H^<$ decreases with increasing *Re* at early times (i.e. $t^* < 8$), which is mainly due to the suppressed viscous effect. For all *Re* cases, $H_d^<$ becomes rather small when $t^* > 8$. Interestingly, it becomes slightly positive at $Re = 4000$. As a result, $H^<$ experiences a minor increase, which, as discussed in Scheeler *et al.* (2014) and Yao *et al.* (2021), is mainly due to the effect of writhe and twist helicity conversions presented for a coiled vortex ring.

As the LR is closely cuddled, its helicity evolution is more complex than that of the TR. The $H^>$ is always negative and decreases initially – suggesting that the contribution of $-h$ in LR becomes larger. Then, $H^>$ increases and asymptotically approaches zero at the late time. In addition, the growth rate increases with *Re* – implying a more rapid dissipation

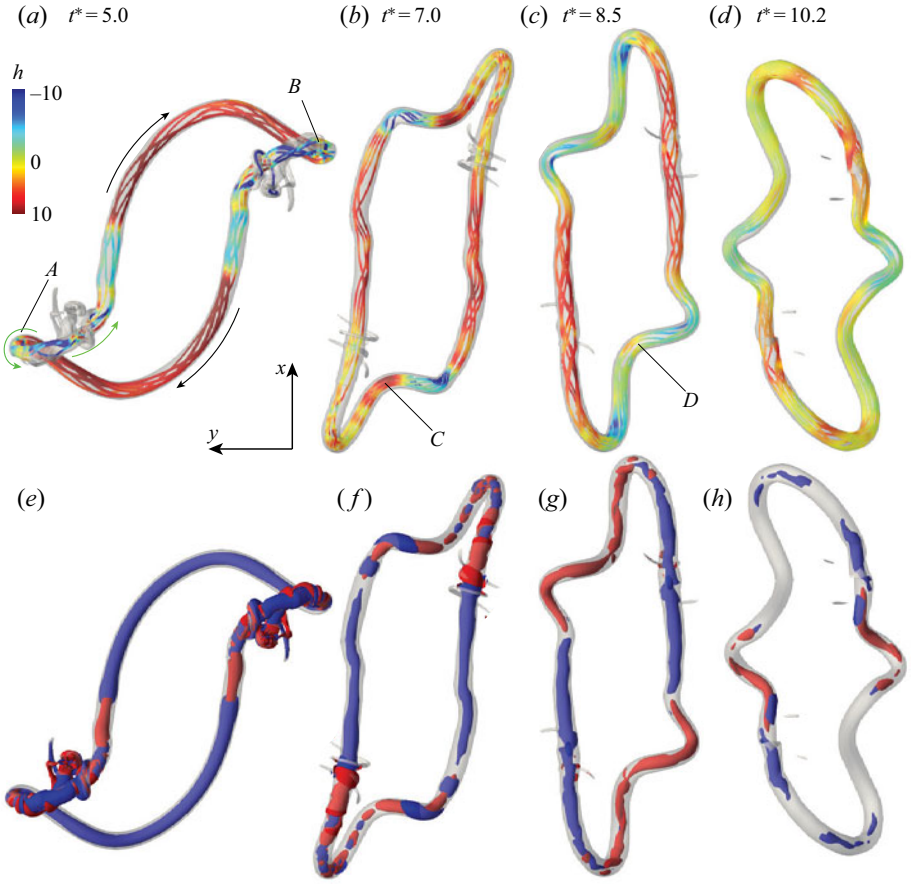

Figure 10. Evolution of flow structures represented by (*a–d*) vortex lines shaded with helicity density $h = \boldsymbol{u} \cdot \boldsymbol{\omega}$ and (*e–h*) helicity dissipation density h_d for the TR after reconnection at $Re = 3000$. Note that red and blue colours denote positive and negative of 5 % of the maximum value, and the transparent (grey) isosurface represents $|\boldsymbol{\omega}| = 0.04\omega_0$.

of negative h at higher Re. By comparing H with $H^>$, it is clear that the decrease and increase of H immediately after reconnection (i.e. $4.5 < t^* < 6$) is mainly caused by the LR. During $6 < t^* < 12$, the decay rates of $H^>$ and $H^<$ is comparable – resulting in a quasi-steady evolution of H. After that, the $H^>$ almost decays to zero, and the evolution of H is mainly governed by $H^<$, which continuously decays with time (figure 3*c*).

Figure 10(*a–d*) further shows the evolution of vortex lines (colour coded by the helicity density h) in TR at several instants after reconnection for $Re = 3000$ with figure 10(*e–h*) displaying the corresponding helicity dissipation density h_d. Note that helicity dissipation is indicated by negative (blue) and positive (red) of h_d in the $+h$ and $-h$ regions, respectively. As the TR is mostly associated with $+h$, vortex lines are mostly right-hand twisted. In addition, the TR is coiled near the two reconnected sites (indicated by A and B in figure 10*a*) with h being positive or negative on each side of the kink structure – resulting from reconnection of two oppositely polarized vortex segments (figure 8). Due to the induced velocities of the kinks, the TR rotates counter-clockwise. In addition, the kink structures also travel counter-clockwise along with the TR through folding/unfolding. The $\pm h$ patches, which propagate along the ring, decay with time due to viscous dissipation.

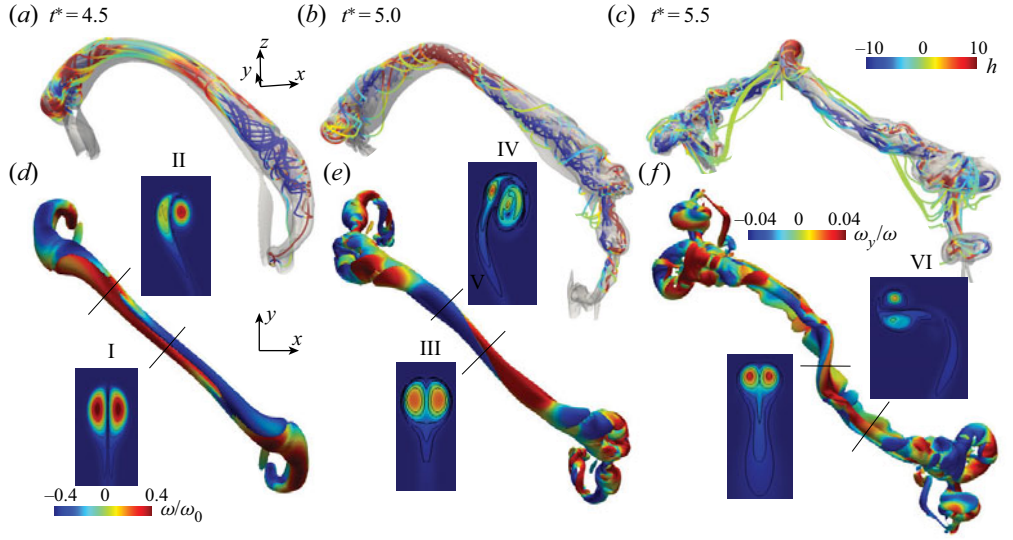

Figure 11. Evolution of the LR represented by (*a–c*) vortex lines shaded with helicity density $h = \boldsymbol{u} \cdot \boldsymbol{\omega}$ and (*d–f*) vorticity isosurface shaded by ω_y helicity dissipation density h_d at $Re = 3000$.

Correspondingly, the vortex lines progressively become untwisted. The regions with strong h have intense h_d of opposite sign – indicating that significant helicity dissipation occurs in the strong helical region. Initially, the region with $-h_d$ is much larger than that of $+h_d$ (figure 10*e*) – consistent with an overall decrease of $H^<$ in the TR (figure 9*a*). The region with positive $+h_d$ enlarges at late times (i.e. $t^* = 8.5$), and becomes comparable to that of $-h_d$ – suggesting the decrease of dissipation of $H^>$. At late times, both $\pm h$ decrease, and h_d is mainly localized in the kink region.

Figures 11(*a*)–11(*c*) show the evolution of LR represented by vortex lines colour coded by the helicity density h at several instants immediately after reconnection for $Re = 3000$. The LR, which results from the recombination of the top parts of the initial vortex rings, is closely touched. The vortex lines inside are strongly twisted, predominately near the ends (i.e. the bridges). In addition, they are oppositely twisted on each side of the bridges. As h is small near the tipping points, the vortex lines there are almost parallel. Due to the self-induction of the curved vortex segments, the LR continuously undergoes reconnection. However, different from what is typically observed for elliptic vortex rings or colliding vortex rings (Kida & Takaoka 1988; Yao & Hussain 2020*c*), here, the two vortex segments collide and reconnect in an asymmetric manner.

The process can be better illustrated by the top view of the vorticity isosurface colour coded by ω_y shown in figure 11(*d–f*) and with adjoining illustrated sketches in figure 12. The two vortex tubes collide with a slight offset, and then the top of one vortex flips over the other (figures 10*d* and 12*b*). Due to skew symmetry, the vortex dipole at the centre (I in figure 11*d*) is still symmetric but becomes asymmetric near the end (II in figure 11*d*). In particular, the core of the left vortex is deformed. Consequently, the initially straight vortex lines become curved, and their induced velocity causes the vortices to be polarized (figure 12*c*): h is positive near the centre and negative near the side – consistent with what is shown in figure 11(*b*). In addition, it further pulls one vortex to the top of the other one – causing the overall twist of the LR (figure 11*e*). In addition, the centre region rotates clockwise – akin to what was observed by Yao & Hussain (2021) for reconnection of

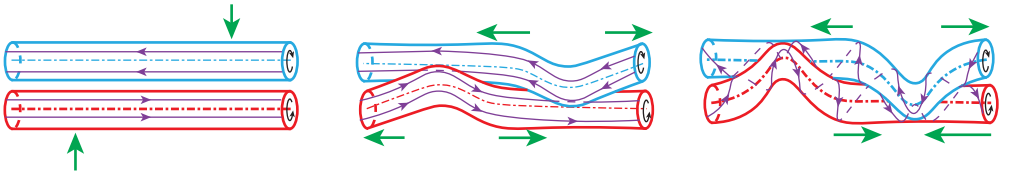

Figure 12. Schematic of the asymmetric reconnection of the LR.

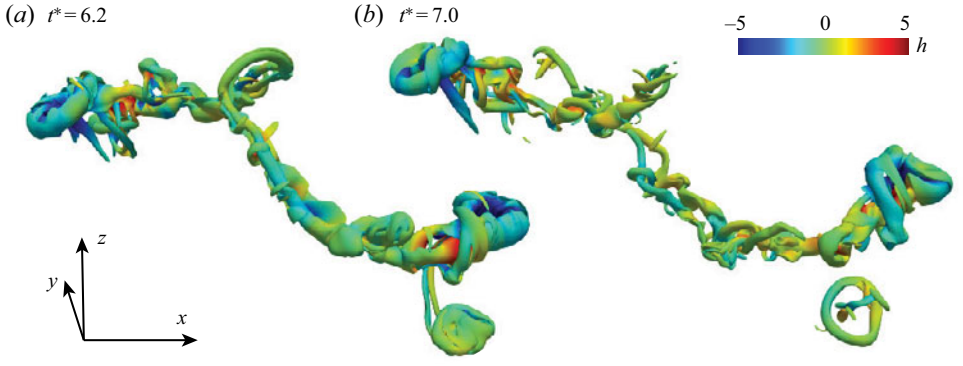

Figure 13. Evolution of flow structures represented by vorticity isosurface at 4 % of maximum initial vorticity ($|\boldsymbol{\omega}| = 0.04\omega_0$) colour coded by helicity density h: (*a*) $t^* = 6.2$ and (*b*) $t^* = 7.0$.

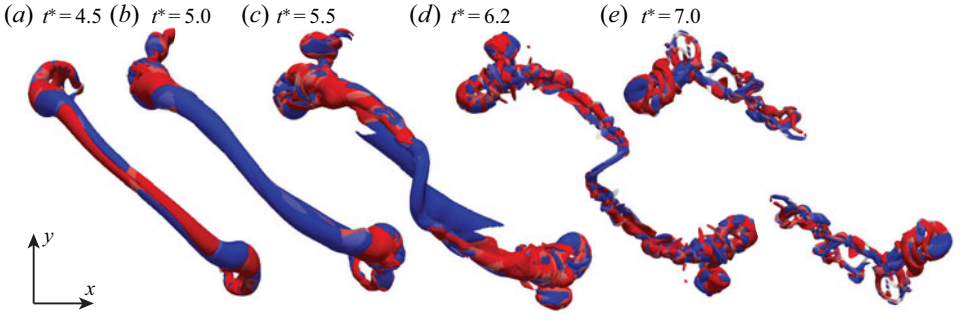

Figure 14. Isosurface of helicity dissipation density h_d for the LR at $Re = 3000$: (*a*) $t^* = 4.5$, (*b*) $t^* = 5.0$, (*c*) $t^* = 5.5$, (*d*) $t^* = 6.2$ and (*e*) $t^* = 7.0$. Note that red and blue colours denote positive and negative of 5 % of the maximum value.

anti-parallel co-polarized vortex tubes. The positive h around the tipping point is rapidly dissipated through reconnection, which is consistent with a decrease of $H^>$ observed in figure 9. Consequently, the LR becomes predominantly $-h$ (figure 10*c*), and its subsequent break up due to instability (figure 13) results in the loss of $-h$; hence, a decrease of $H^>$.

Finally, figure 14 shows the isosurfaces of helicity dissipation density h_d for the LR at several instants. Initially, $\pm h_d$ appears alternatively – which is opposite to the distribution of h shown in figure 11. Then, as the central region becomes right-hand twisted, h_d becomes predominantly negative – consistent with the decrease of $H^>$. At the late time, regions with $+h_d$ increase and become comparable to that of $-h_d$. Both $\pm h_d$ occurs at small scales – implying the existence of a forward helicity cascade along with the energy cascade.

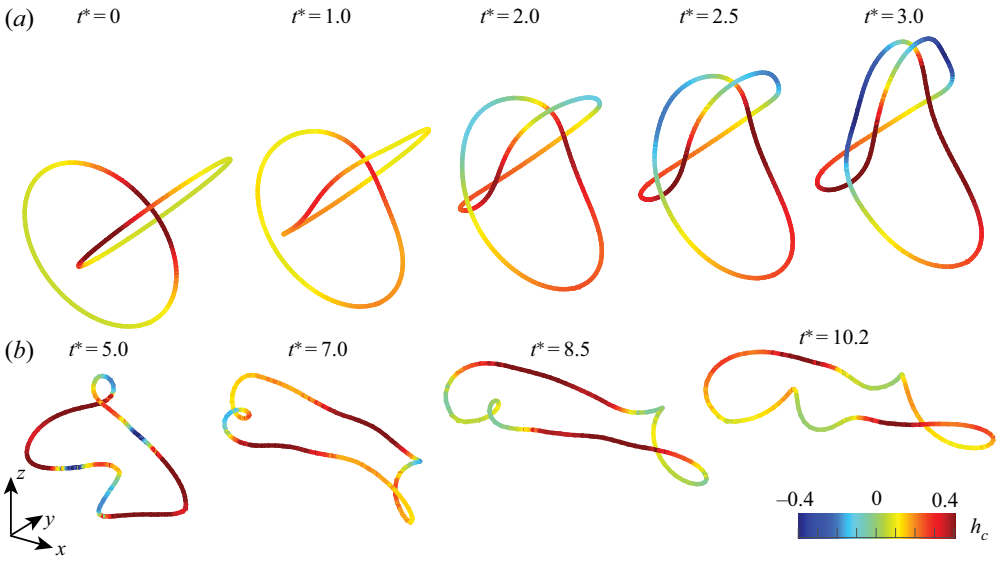

Figure 15. Evolution of extracted vortex axis (shaded with centreline helicity density $h_c = \boldsymbol{u} \cdot \boldsymbol{T}$) for (*a*) vortex rings before reconnection and (*b*) the TR after reconnection at $Re = 3000$.

5. Topological aspects of helicity dynamics

5.1. *Properties of vortex centrelines*

In this section, we examine the topological dynamics of the vortex links in terms of the vortex core centrelines (axes). Following Yao *et al.* (2021), we use the method developed by Levy, Degani & Seginer (1990) based on the normalized helicity density $\boldsymbol{u} \cdot \boldsymbol{\omega}/(|\boldsymbol{u}||\boldsymbol{\omega}|)$ and implemented in Paraview by Sadlo *et al.* (2019) to identify vortex centrelines. The method assumes that the angle between the velocity and vorticity vectors is typically minimal near the axis and can filter out the regions of low vorticity as well as regions of high vorticity but low velocity (Levy *et al.* 1990). It has been demonstrated to successfully extract the vortex axis, except for the period when reconnection occurs and the vortex axis is hardly defined (Yao *et al.* 2021). Figure 15 displays the evolution of the axes for two vortex rings before reconnection and for the TR after reconnection at $Re = 3000$. Note that, as the LR after reconnection is closely cuddled with irregular core shape (figure 11) and rapidly breaks up afterward, its centreline is rather difficult to extract and, therefore, is not included.

Several interesting quantities can be measured based on the tracked vortex axis. The first one is the length of the vortex centreline l_c. Figure 16 shows the evolution of lengths for the vortex ring before reconnection and the TR after reconnection (normalized by the initial length of a single vortex ring $2\pi R_0$). Consistent with what was observed by Scheeler *et al.* (2014), the length $l_c(t)$ before reconnection continuously increases and is almost identical for different Re. During reconnection, the rate of growth of $l_c(t)$ increases with Re, which is due to a larger vortex stretching at higher Re. After reconnection, $l_c(t)$ for the LTR remains almost constant and, interestingly, is approximately twice the initial length of the vortex ring.

The moment of vorticity for a vortex knot in a fluid at rest at infinity is related to the impulse (Batchelor 2000). As a theoretical estimation for the thin vortex filament,

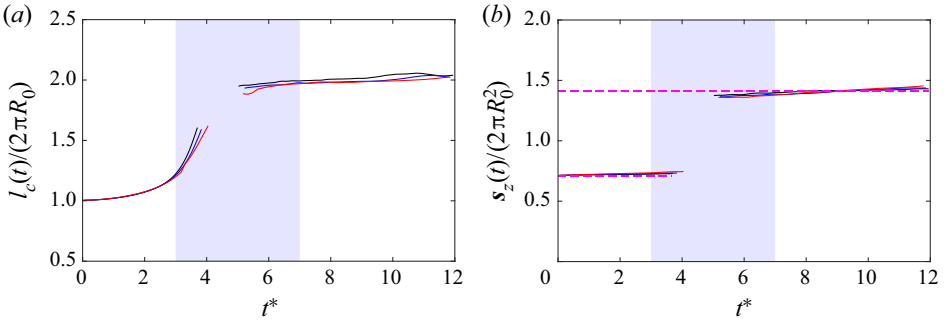

Figure 16. Time evolution of (*a*) normalized length $l_c/(2\pi R_0)$ and (*b*) the third components of the directed area enclosed by the vortex centrelines S_3 for the vortex ring before reconnection, and LTR after reconnection.

substituting $\boldsymbol{\omega}\,\mathrm{d}V = \Gamma\,\mathrm{d}\boldsymbol{c}$ in (2.2) yields

$$\boldsymbol{I} = \Gamma \boldsymbol{S}, \tag{5.1}$$

where $\boldsymbol{S} = \oint_c \boldsymbol{c} \times \mathrm{d}\boldsymbol{c}/2$ is the directed area enclosed by the curve (Wu, Ma & Zhou 2007). Equation (5.1) provides a geometric way to estimate the momentum by computing the individual momentum components from direct measurements of the area regions obtained by planar projections of the vortex axis (Zuccher & Ricca 2019).

The vortex link here has an initial impulse $\boldsymbol{I} = (0, 0, \sqrt{2}\pi)$. Figure 16(*b*) shows the evolution of the third component of $\boldsymbol{S}$, i.e. S_3. Note that the other two components are negligible for all times and hence are not shown. Before reconnection, S_3 visually collapses for all *Re* cases and slightly increases with time. As $\boldsymbol{I}$ is invariant, the increase of S_3 is mainly due to the decrease in circulation Γ through viscous cross-diffusion. The difference between the calculated value and the theoretical prediction (based on constant circulation assumption) is within 1 % for all *Re* cases. After reconnection, S_3 for TR also slightly increases with time, and is very close to the theoretical value for the whole flow system. This suggests that the moment of vorticity is mainly carried by the TR – consistent with the flow visualization in figure 11 showing that the area for the LR projected in the *x*–*y* plane is negligible.

5.2. *Centreline helicity*

For sufficiently thin vortex tubes with minimal vorticity variation across the cross-section, the global helicity is encoded completely along the centreline of the vortex tube (Bretherton 1970; Scheeler *et al.* 2017). Hence,

$$H_c = \sum_i \Gamma_i \oint_{C_i} \boldsymbol{u}(s) \cdot \boldsymbol{T}(s)\,\mathrm{d}s, \tag{5.2}$$

where $h_c = \boldsymbol{u} \cdot \boldsymbol{T}$ is the centreline helicity density and $\boldsymbol{T}$ denotes the unit tangential vector along the vortex centreline C. Equation (5.2) provides an easy way for estimating the helicity of the flow without the need for measuring the full velocity and vorticity fields. The value of H_c has also been employed to represent the link and writhe helicities, which is based on the assumption that the twist helicity is small and can be dissipated rather rapidly, particularly for a very thin vortex (Scheeler *et al.* 2014).

Figure 17 compares H_c and H for the vortex rings before reconnection and for TR after reconnection. Note that the circulation Γ is assumed to remain the same as the initial value,

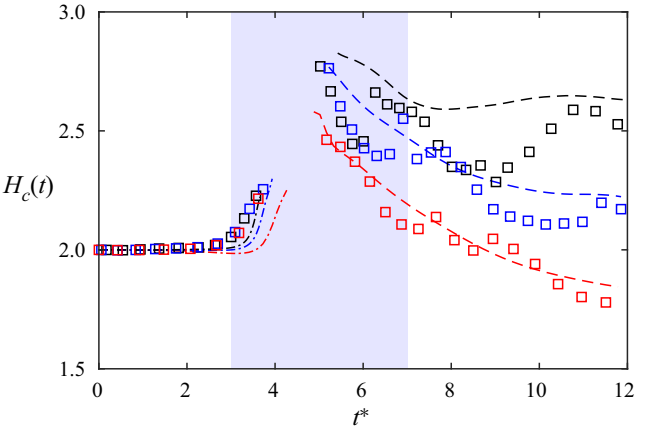

Figure 17. Time evolution of the centreline helicity H_c (square) and helicity (lines) for the vortex rings before reconnection and for TR after reconnection at $Re = 2000$ (red), 3000 (blue) and 4000 (black).

and H in TR is calculated based on (4.3*a*,*b*). Before reconnection, H_c is almost identical to H – confirming that H_c is a reasonably good approximation for H. After reconnection, H_c experiences oscillations, which are due to the growth and annihilation of the axial flows along the vortex ring. In addition, the agreement between H_c and H deteriorates with increasing Re, which, as discussed in Yao *et al.* (2021), is mainly due to the following two reasons. First, reconnection induces strong core deformation near the interaction region, such as forming vortex sheets. Consequently, the vortex core becomes irregular with a substantial vorticity variation, especially at higher Re. Second, the threads, which wrap around the TR, are polarized and contain a certain amount of h, which is somehow excluded by H_c. Therefore, H_c cannot be employed to approximate H immediately after reconnection. Due to viscous diffusion, the vortex core of TR would become regular (i.e. circular) again, and the threads become weaker, H_c would eventually approach H. But the time it takes seems to significantly increase with Re.

5.3. *Gauss linking and self-link numbers, writhe and torsion twist*

Here, we attempt to provide a topological interpretation of the helicity dynamics. The definition of the geometric and topological quantities presented in (1.1) are summarized here. The Gauss linking number between the vortices i and j is obtained by the double integral over the axes

$$L_{k,ij} = \frac{1}{4\pi}\int_{C_i}\int_{C_j}\frac{\boldsymbol{X}_i - \boldsymbol{X}_j}{|\boldsymbol{X}_i - \boldsymbol{X}_j|^3}\cdot(\mathrm{d}\boldsymbol{X}_i \times \mathrm{d}\boldsymbol{X}_j), \tag{5.3}$$

where $\boldsymbol{X}_i$ and $\boldsymbol{X}_j$ denote the position vectors of a point on C_i and C_j, respectively. The total Gauss linking number L_k, which takes integer values only, provides a measure of the degree of linking of two (or more) disjoint vortices.

The writhe is defined as

$$Wr_i = \frac{1}{4\pi}\int_{C_i}\int_{C_i}\frac{\boldsymbol{X}_i - \boldsymbol{Y}_i}{|\boldsymbol{X}_i - \boldsymbol{Y}_i|^3}\cdot(\mathrm{d}\boldsymbol{X}_i \times \mathrm{d}\boldsymbol{Y}_i), \tag{5.4}$$

where $\boldsymbol{X}_i$ and $\boldsymbol{Y}_i$ denote two distinct points on the same vortex axis C_i. Note that $W_{r,i}$ is a global geometric property of C_i and is always zero if C_i is a plane curve (Zuccher

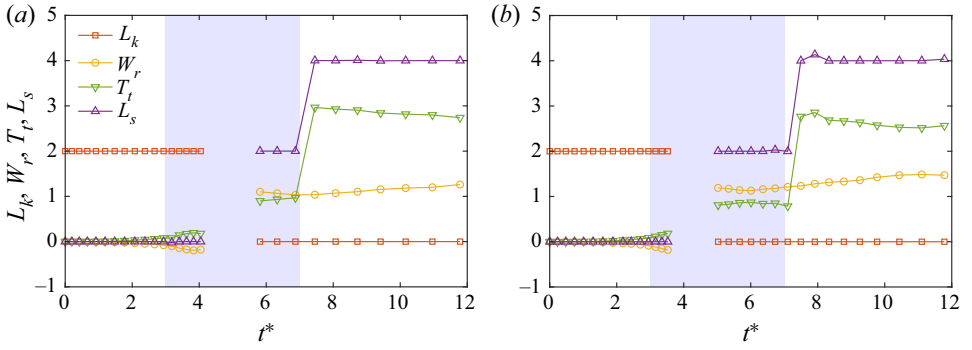

Figure 18. Time evolution of total Gauss link (L_k), writhe (W_r), torsion twist (T_t) and self-link (L_s) for (a) $Re = 2000$ and (b) 4000.

& Ricca 2017). Since writhe takes into account distortion, it is often a good indicator of three-dimensional folding of the vortex.

The twist is defined by the rate of rotation of the ribbon unit vector around the curve C_i, and it can be further decomposed into torsion T_t and intrinsic twist T_i, given respectively by

$$T_t = \frac{1}{2\pi} \int_{C_i} \tau(s)\, \mathrm{d}s, \tag{5.5}$$

and

$$T_i = \frac{1}{2\pi} \int_{C_i} \xi(s)\, \mathrm{d}s, \tag{5.6}$$

with $\tau(s)$ and $\xi(s)$ denoting local torsion and the rate of azimuthal change along C_i. Note that the sum of W_r and T_t is the self-linking number L_s, which takes integer values only (Pohl 1968).

Figure 18(a,b) shows the total Gauss link (L_k), writhe (W_r), torsion twist (T_t) and self-link (L_s) for the vortex links before reconnection and the LTR after reconnection at $Re = 2000$ and 4000, respectively. As the numerical computation of writhe and torsion is very sensitive to small-scale noise, a local smoothing filter similar to that used in Scheeler *et al.* (2014) and Yao *et al.* (2021) is applied to the raw extracted vortex centreline. Initially, L_k is equal to two and remains unchanged before reconnection, as $L_{k,12} = L_{k,21} = +1$. In addition, W_r is initially zero and slightly decreases before reconnection, which is consistent with what was observed by Zuccher & Ricca (2017) for quantum vortex links. During this period, T_t is equal to $-W_r$; consequently, L_s remains zero. In addition, the variation of W_r and T_t only weakly depends on Re.

During reconnection, when the vortex rings undergo dramatic changes in topology, all these quantities are expected to experience abrupt changes. As two vortices untie, L_k decreases to zero after reconnection. The W_r value for TR becomes positive and slowly varies with time, and T_t also jumps through reconnection; consequently, L_s for TR becomes 2 after reconnection. Note that the integer L_s jumps discontinuously through ± 1 as a curve passes through a configuration containing a point of inflexion (Moffatt & Ricca 1992). Owing to the bi-symmetry of the vortex links, the curve deformation during the reconnection involves passage through two inflexional configurations. This explains why L_s becomes 2 for the TR. For the same reason, L_s for the LR is also speculated to be 2 – causing a doubling of the total linking number ($L_k + L_s$) during reconnection. This argument can be confirmed in Appendix B for the smaller angle case (i.e. $\alpha = 30^\circ$).

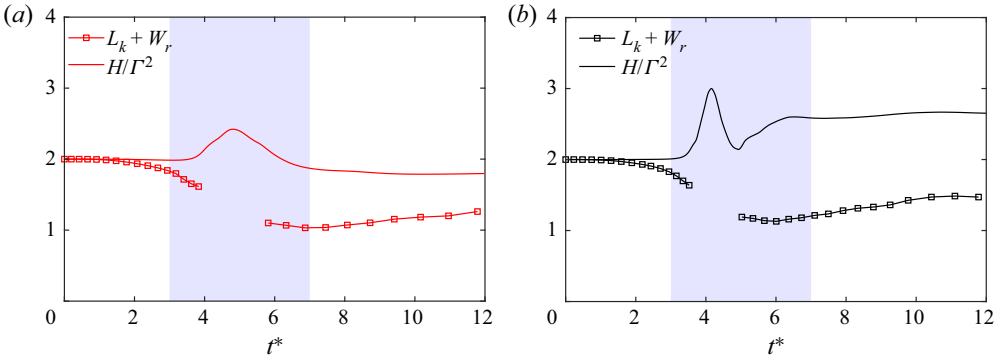

Figure 19. Comparison between H/Γ^2 and the sum of Gauss link and writhe ($L_k + W_r$) for (a) $Re = 2000$ and (b) 4000.

As Re increases, W_r mildly increases, and T_t decreases. Note that T_t for TR further jumps around $t^* \approx 7$, which causes L_s to increase from 2 to 4. As the numerical calculation of T_t (and also L_s) is very sensitive at the inflexional configuration for which T_t is discontinuous by ± 1, the jump of T_t suggests that additional inflexion points develop in the TR, which might be due to the influence of the other structures. Hence, in viscous flows, T_t (also L_s) is also not conserved during the evolution.

Figure 19(a,b) shows the sum of L_k and W_r for the vortex links before reconnection and for the TR after reconnection at $Re = 2000$ and 4000, respectively. Here, H/Γ^2 is also included for comparison. The behaviour of $L_k + W_r$ here is similar to that observed in experiments in classical fluids by Scheeler *et al.* (2014) and also simulations in superfluids by Proment & Krstulovic (2020). Before reconnection, $L_k + W_r$ continues to decrease. Although we are unable to resolve W_r during reconnection and that for the LR, it seems that the evolution of $L_k + W_r$ is continuous through reconnection. It is confirmed in Appendix B for the $\alpha = 30^\circ$ case, where $L_k + W_r$ for the total two rings varies continuously through reconnection – consistent with the claim made by Laing, Ricca & Sumners (2015).

From figure 19, it is clear that that twist, which can be approximated as the difference between H/Γ^2 and $L_k + W_r$, is the main contributor to the complex helicity dynamics observed in figure 3. As both the experimental work by Scheeler *et al.* (2014) and the numerical work by Kivotides & Leonard (2021) only considered $L_k + W_r$, the conservation of helicity is based on the assumption that the twist generated through reconnection is small and can be rapidly damped through viscous dissipation. From our DNS results and also the previous works by Zhao *et al.* (2021) and Zhao & Scalo (2021), this assumption is trivially invalid. The contribution of T_w (especially T_i) to H is very significant during and after reconnection and enlarges with increasing Re. Hence, it is expected that twist would play a more significant role at very high Re.

6. Concluding remarks

The DNS of two slender vortex rings in Hopf-link configuration is performed at three different Re (i.e. 2000, 3000 and 4000). The global helicity H, although remaining constant before reconnection, increases during reconnection, followed by a rapid decay – both the growth and decay rates increase with Re. Before eventually decaying at the very late time, H further increases after reconnection and reaches an almost quasi-plateau at high Re. In addition, the asymptotic value of the plateau increases with Re, suggesting that H is

not conserved at very high Re – contrasting with the previous findings by Scheeler *et al.* (2014) and Kivotides & Leonard (2021). We further discover that significant amounts of positive and negative twist helicities are simultaneously generated before and during reconnection, and the difference in their decay rates is the main reason for the increase of H during reconnection. Different from what was observed for a trefoil knotted vortex (Yao *et al.* 2021; Zhao & Scalo 2021), H at higher Re experiences strong oscillation, which is attributed to the subsequent reconnection and break-up of the closely cuddled LR.

The topological aspects of the helicity dynamics are also examined. The centreline helicity, calculated as $H_c = \sum_i \Gamma_i \oint_{\mathcal{C}_i} \boldsymbol{u} \cdot \boldsymbol{T}(s)\, \mathrm{d}s$, is found to be a good approximation for H only before reconnection. It deviates from H after reconnection, particularly at high Re. The writhe, W_r, is initially zero, continuously decreases before reconnection and experiences a sudden jump for the newly formed ring immediately after reconnection. However, the sum of link and writhe $(L_k + W_r)$ seems to vary continuously during reconnection – implying that link is mostly converted to writhe during reconnection. But during this conversion process, significant amount of twist (T_w) is generated. Our results also clearly show that T_w, which continuously increases with Re, plays a significant role in the helicity dynamics, particularly at very high Re. It is worth mentioning that the initial configuration considered here is too idealized such that two reconnections occur simultaneously due to symmetry. It would be interesting to examine how the flow evolution and helicity dynamics are altered in a more complicated geometry, which is more generic in real flows.

Supplementary movie. Supplementary movie is available at https://doi.org/10.1017/jfm.2022.532.

Acknowledgements. Computational and visualization resources provided by Texas Tech University HPCC, TACC Lonestar, Frontera, and Stampede2 under XSEDE are acknowledged.

Declaration of interest. The authors report no conflict of interest.

Author ORCIDs.
Jie Yao https://orcid.org/0000-0001-6069-6570;
Weiyu Shen https://orcid.org/0000-0003-4385-8835;
Yue Yang https://orcid.org/0000-0001-9969-7431;
Fazle Hussain https://orcid.org/0000-0002-2209-9270.

Appendix A. Grid convergence analysis

We provide here a grid sensitivity analysis for Reynolds numbers $Re = 2000$ and 4000. For each Re, three different grid resolutions are tested, namely, $N^3 = 512^3$, 768^3 and 1024^3 for $Re = 2000$; and $N^3 = 1024^3$, 1536^3 and 2048^3 for $Re = 4000$. Figures 20(*a*) and 20(*b*) show the time evolution of enstrophy Ω and helicity H for these cases. The good collapse of Ω indicates that grid resolutions we employed in the main text are sufficient to capture the small scales generated during the reconnection process. In addition, good agreements for H among different resolutions are also observed, particularly at earlier times. The small difference at the late times after reconnection might be due to the insufficiency in capturing the strong axial velocity associated with the twisted structures. Furthermore, to examine the domain size effect, an additional simulation with domain size $(3\pi)^3$ is performed for $Re = 2000$ with $N^3 = 1024^3$, which yields exactly the same results as the smaller domain case – confirming the adequacy of the domain size chosen in the main study.

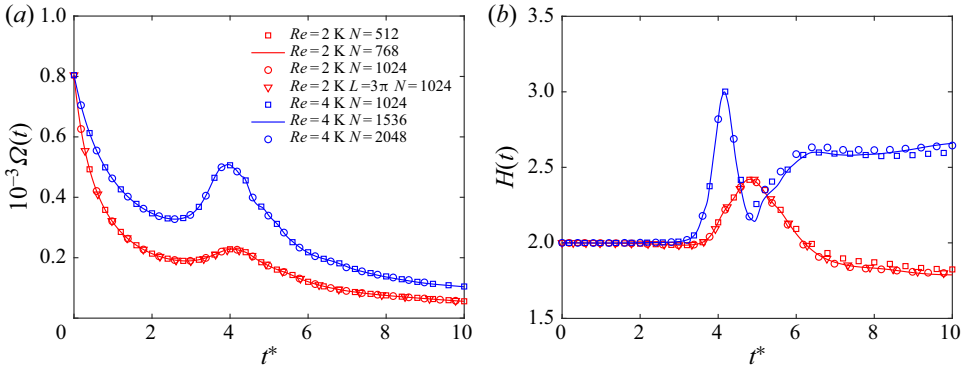

Figure 20. Time evolution of (*a*) enstrophy Ω and (*b*) global helicity H for $Re = 2000$ (red), 4000 (blue) with different grid resolutions and domain sizes.

Appendix B. Evolution of the link of vortex rings at a different angle

In this section, we consider the evolution of the link of two vortex rings at a smaller angle (i.e. $\alpha = 30^\circ$ in figure 1). Two different Re (i.e. 2000 and 4000) are considered, and the grid resolutions for each Re are identical to those used in the main text. Figure 21(*a*) shows the time progression of flow structures visualized based on vorticity magnitude isosurface $|\boldsymbol{\omega}| = 0.04\omega_0$ for $Re = 2000$. Similar to figure 2, the two rings become perturbed and become locally anti-parallel before reconnection. Note that, as the two rings are initially closer, the reconnection happens earlier than in the $\alpha = 90^\circ$ case. After two simultaneous reconnections, the vortex link unties to form two distinct coiled vortex rings – quite different from that for the $\alpha = 90^\circ$ case. These two rings then move upward as they rotate. The whole process is quite similar to that observed in Yao *et al.* (2021) for the trefoil knotted vortex. Figure 21(*b*) shows the corresponding time progression of the vortex centrelines, which captures well the evolution of the vortex rings before and after reconnection.

The topological quantities (i.e. L_k, W_r, T_t and L_s) calculated based on the extracted vortex centrelines are shown in figure 22(*a*,*b*) for $Re = 2000$ and 4000, respectively. Before reconnection, the evolution of all these quantities is quite similar to that for the $\alpha = 90^\circ$ case. After reconnection, L_k again becomes zero. The value of W_r for both rings becomes positive and slowly varies with time. In particular, similar to what is discussed in Yao *et al.* (2021), W_r continuously increases/decreases for the LR/TR – as the LR and TR are being stretched and compressed, respectively. In addition, the TR has a larger W_r, which is consistent with what is shown in figure 21 where the TR has more three-dimensional folding. The value of T_t also abruptly increases for both rings during reconnection, but this time, T_t for the LR is larger than that of the TR. Hence, T_t is not conserved through reconnection, which is quite different from what was shown in Laing *et al.* (2015) for the ideal anti-parallel reconnecting segments. Consequently, after reconnection, $L_s(\equiv W_r + T_t)$ for each ring remains constant all the time and is equal to the value of L_s. This suggests that the total linking number $(L_k + L_s)$ doubles during reconnection, which is consistent with our previous findings for a trefoil knotted vortex (Yao *et al.* 2021). Note that whether such doubling of $L_k + L_s$ through reconnection is universal for various configurations needs further investigation.

Finally, figure 23 compares H/Γ^2 with $L_k + W_r$ at $Re = 2000$ and 4000. Different from the $\alpha = 90^\circ$ case, H slightly increases before reconnection, which is probably due to the

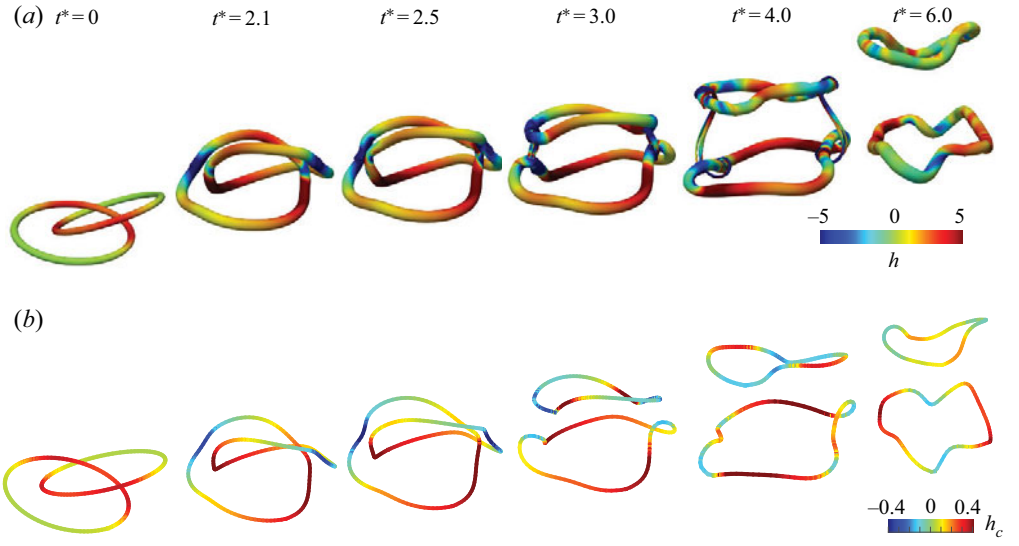

Figure 21. Time evolution of flow structures represented by (*a*) vorticity isosurface $|\boldsymbol{\omega}| = 0.04\omega_0$ (shaded with helicity density $h = \boldsymbol{u}\cdot\boldsymbol{\omega}$) and (*b*) vortex centrelines (shaded with centreline helicity density $h_c = \boldsymbol{u}\cdot\boldsymbol{T}$) for vortex link with $\alpha = 30^\circ$ at $Re = 2000$.

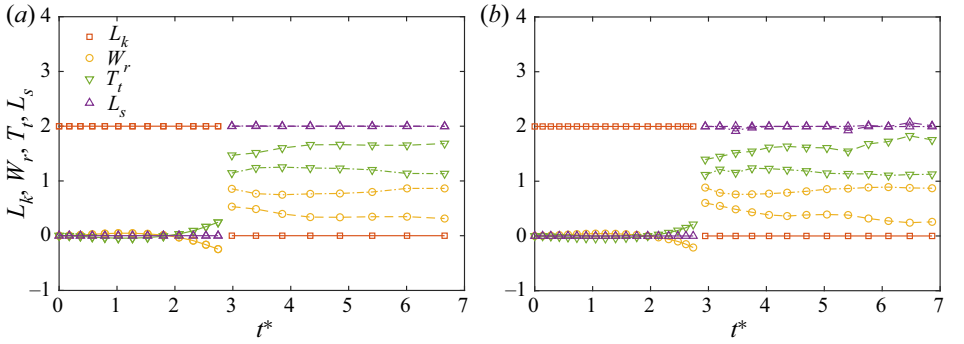

Figure 22. Time evolution of Gauss link (L_k), writhe (W_r), torsion twist (T_t) and self-link (L_s) for vortex link with $\alpha = 30^\circ$ at (*a*) $Re = 2000$ and (*b*) 4000.

strong mutual interaction of the vortex rings as they are closer at smaller α. Similar to what is observed for the $\alpha = 90^\circ$ case, H/Γ^2 rapidly grows during reconnection and then decreases – suggesting that the increase of H through reconnection is quite universal. However, the rapid decay of H immediately after reconnection observed for the $\alpha = 90^\circ$ case does not occur here – further implying that it is mainly due to the evolution of the LR. The value of $L_k + W_r$ also increases at the earlier time and becomes slightly higher than H, indicating the generation of negative twist helicity. It then decreases before the reconnection and rapidly drops during the reconnection. And the variation of $L_k + W_r$ seems to be continuous – indicating that the link is mainly converted to writhe during the unlinking process. The decay of $L_k + W_r$ slightly decreases with increasing Re. After reconnection, the variation of $L_k + W_r$ with time becomes limited and only has some slight oscillations, which is consistent with what was observed in Yao *et al.* (2021) for the trefoil knotted vortex case. Again, the difference between H/Γ^2 and $L_k + W_r$ increases with

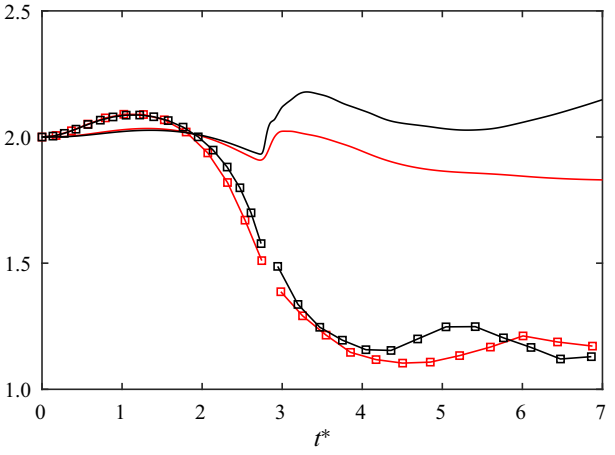

Figure 23. Comparison between H/Γ^2 (solid line) and the sum of Gauss link and writhe $L_k + W_r$ (square) for vortex link with $\alpha = 30^\circ$ at $Re = 2000$ (red) and $Re = 4000$ (black).

Re – suggesting the more significant generation of T_w at higher Re. Due to the dissipation of T_w, H/Γ^2 and $L_k + W_r$ would eventually collapse, but the time it takes becomes much longer at higher Re.

Appendix C. Helicity dynamics in asymmetric reconnection of colliding vortex rings

We demonstrate that the symmetry breaking in the generation of $\pm h$ during asymmetric vortex reconnection causes significant helicity variation, by comparing DNS results in symmetric and asymmetric collision of two vortex rings. The symmetrical initial configuration (figure 24*a*) is set by the parameter equations

$$\begin{cases} c_{x,\pm}(\zeta) = \dfrac{\sqrt{2}}{2}\cos(\zeta) \mp \varepsilon, \\ c_{y,\pm}(\zeta) = -\sin(\zeta), \\ c_{z,\pm}(\zeta) = \pm\dfrac{\sqrt{2}}{2}\cos(\zeta), \end{cases} \tag{C1}$$

where $\varepsilon = 0.85$ denotes the separation distance between two rings. The asymmetric initial configuration (figure 24*b*) is set by slightly rotating a ring by $\theta = \pi/8$ around a diameter on the $x - z$ plane. The parametric equations for the rotated ring are

$$\begin{cases} c_{x,+}(\zeta) = \dfrac{\sqrt{2}}{2}[\cos(\zeta) + \sin(\zeta)\sin(\theta)] - \varepsilon, \\ c_{y,+}(\zeta) = -\sin(\zeta)\cos(\theta), \\ c_{z,+}(\zeta) = \dfrac{\sqrt{2}}{2}[\cos(\zeta) - \sin(\zeta)\sin(\theta)]. \end{cases} \tag{C2}$$

The other geometric parameters in these two cases are the same as those for the Hopf link, i.e. $R_0 = 1$, $\Gamma_0 = 1$ and $\sigma = 1/(16\sqrt{2\pi}) \approx 0.025$. The DNS with the initial conditions in (C1) and (C2) is performed at $Re = 2000$ with $N^3 = 768^3$ grid points.

The time evolutions of the symmetric and asymmetric vortex ring collisions in figure 25(*a*,*b*) look quite similar. The two unlinked vortex rings are reconnected into a coiled vortex ring. During the reconnection, two bridges separate outwards, along with

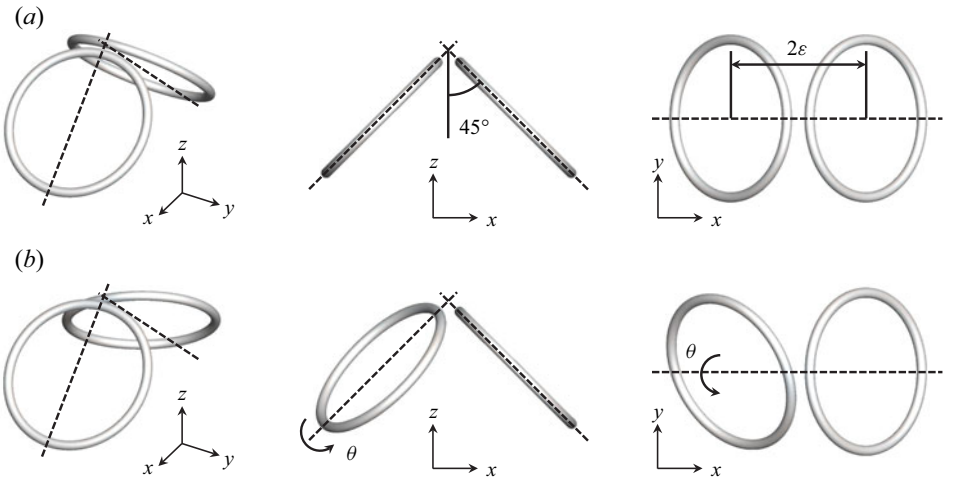

Figure 24. Initial (*a*) symmetric and (*b*) asymmetric configurations of a pair of vortex tubes represented by the vorticity isosurface at 4 % of maximum initial vorticity.

threads stretching upwards. On the other hand, the subtle difference in the structural evolutions between symmetric and asymmetric cases is compared in figure 25(*c*,*d*), focusing on the small region of the bridge and adjacent threads. We can clearly observe the uneven generations of h for the main vortex tube and threads during the asymmetric reconnection. In particular, the pair of threads generate strong opposite helicity densities with significantly different magnitudes. On the contrary, the symmetry is preserved in the generation of $\pm h$ during the symmetric reconnection. Figure 26 plots the time evolution of H, H^+ and H^- in symmetric and asymmetric reconnections. Similar to figure 6 for the Hopf link, both $|H^+|$ and $|H^-|$ surge during the reconnection. In the symmetric reconnection, the identical growths of $|H^+|$ and $|H^-|$ cancel each other, so H is conserved. In the asymmetric reconnection, the relatively small difference in the growths of $|H^+|$ and $|H^-|$ in the skewed collision leads to the notable fluctuation of H.

Figure 27(*a*,*b*) further shows the difference for the topological helicity decomposition in symmetric and asymmetric reconnections, respectively. In the former case, the positive and negative writhing or twisting of the perfectly symmetric vortex tube is completely cancelled out in the evolution. In the latter case, in contrast, the contacting vortex tubes are not strictly anti-parallel, leading to the changes in writhing and twisting and the fluctuation of H.

Appendix D. Effects of the vortex tube thickness

It is well known that the tube thickness σ of the vortex ring affects its self-induced velocity and, hence, its evolution. As shown in Yao & Hussain (2020*b*), σ also plays an important role in the reconnection process, i.e. the reconnection time and rate. Most importantly, the decay rate of helicity is strongly influenced by σ. Therefore, in this appendix, we examine the effect of σ on the helicity evolution of the linked vortex rings by conducting an additional simulation with smaller initial tube thickness (i.e. $\sigma_0 = 1/(32\sqrt{2\pi})$) at $Re = 2000$ on $N^3 = 1536^3$ grid points.

Figure 28(*a*) compares the evolutions of H, H^+ and H^- between the $\sigma_0 = 1/(16\sqrt{2\pi})$ and $1/(32\sqrt{2\pi})$ cases. It is clear that all these quantities follow similar trends between

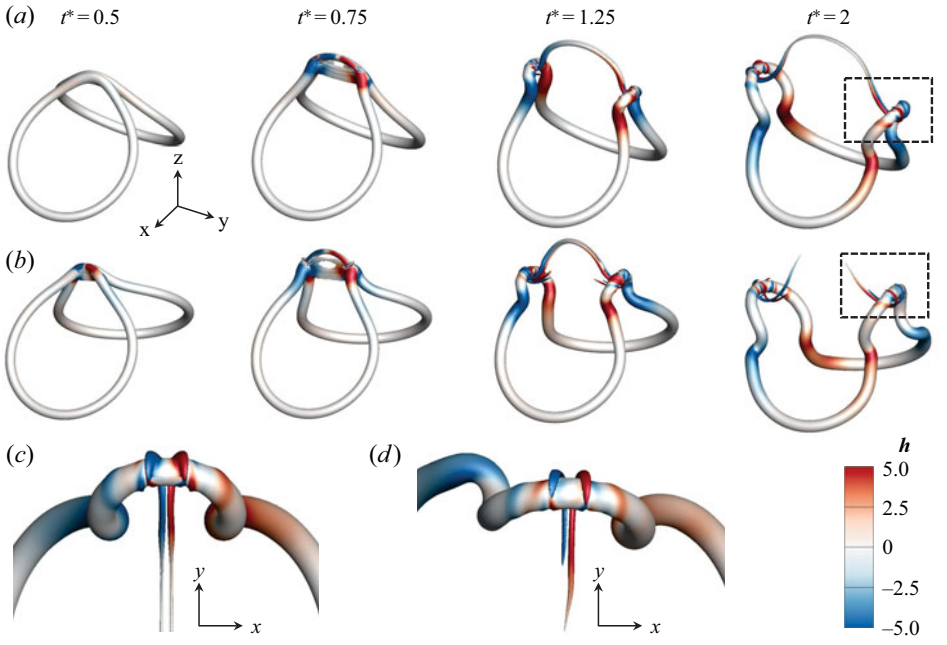

Figure 25. Time evolution of the isosurface of $|\boldsymbol{\omega}| = 0.04\omega_0$ shaded by the helicity density in (*a*) symmetric and (*b*) asymmetric cases; close-up top views of the vortex structure after (*c*) symmetric and (*d*) asymmetric reconnections at $t^* = 2$.

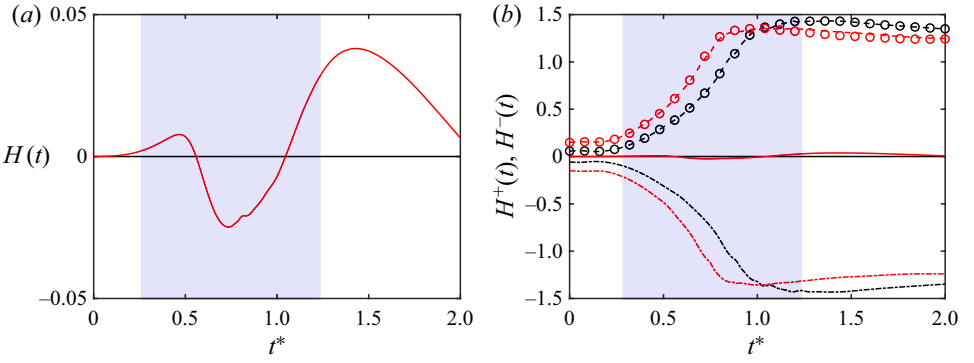

Figure 26. Time evolution of (*a*) H (solid line), (*b*) H^+ (dashed line) and H^- (dash-dotted line) for symmetric (black) and asymmetric (red) cases. The circles denote $-H^-(t)$.

these two cases, with the only difference being that they surge earlier for the smaller tube thickness (i.e. $\sigma_0 = 1/(32\sqrt{2\pi})$) case, which is due to a larger convective velocity and, hence, an earlier reconnection. A good agreement between these two cases can also be observed for the $L_k + W_r$, particularly before reconnection (figure 28*b*) – suggesting that the helicity dynamics is less sensitive to σ_0.

Note that the similar evolution of helicity between these two different σ_0 cases is somehow not unexpected. In viscous flows, the vortex tube thickness generally grows as $\sigma = \sqrt{\sigma_0^2 + 2\nu t}$. Figure 29 shows the time evolution of σ for different σ_0 and ν cases. For initially small tube thickness σ_0, the viscous effect soon becomes the dominant

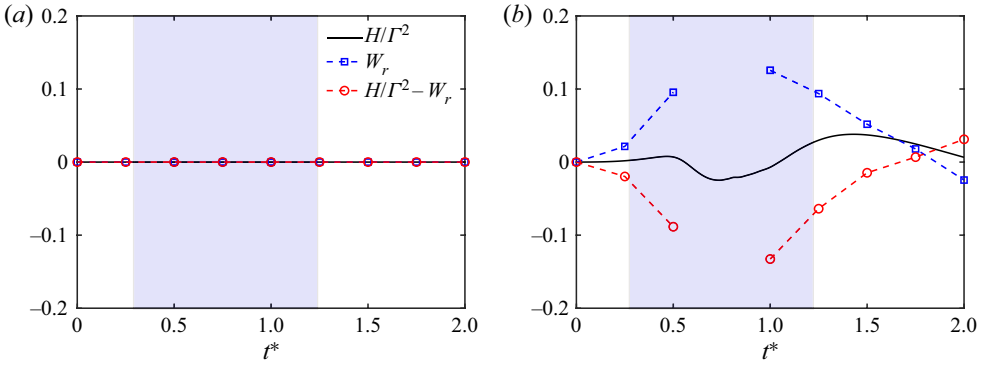

Figure 27. Time evolution of H/Γ^2 and the topological helicity decomposition in (*a*) symmetric and (*b*) asymmetric reconnection cases.

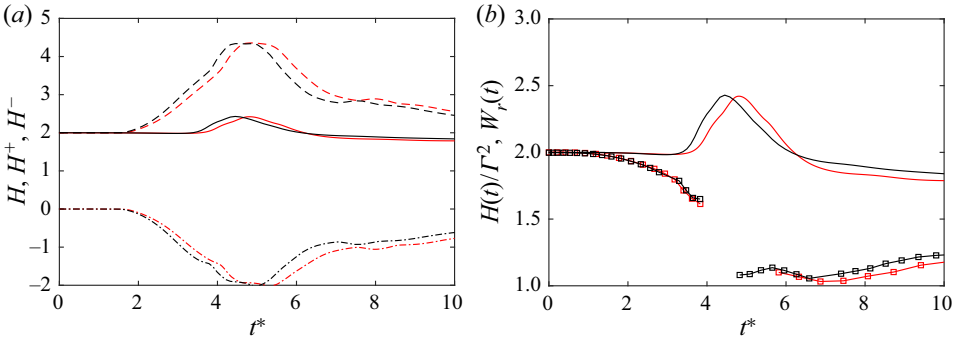

Figure 28. Time evolution of (*a*) H (solid line), H^+ (dashed line) and H^- (dash-dotted line) and (*b*) $L_k + W_r$ (square) for $\sigma_0 = 1/(16\sqrt{2\pi})$ (red) and $\sigma_0 = 1/(32\sqrt{2\pi})$ (red) cases at $Re = 2000$.

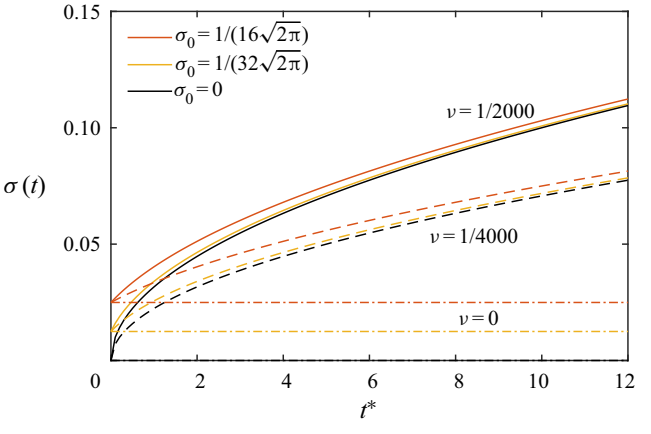

Figure 29. Time evolution of the vortex tube thickness σ for different σ_0 and ν cases.

contribution to σ for the large ν case. Consequently, the difference of σ between different σ_0 becomes smaller. Interestingly, at $\nu = 1/2000$, the evolution of σ for $\sigma_0 = 1/(32\sqrt{2\pi})$ is also very close to the case with zero initial tube thickness (i.e. $\sigma_0 = 0$), which implies that the helicity evolution at $Re = 2000$ would still be quite similar to that shown in

figure 28 for even smaller σ. Figure 29 also shows that the relative difference in σ increases with decreasing ν – suggesting that the flow evolution and the associated helicity dynamics between different σ_0 might be quite different at high Re. However, due to the spatial requirement for resolving the fine vortex core and small scales generated during reconnection, it is currently rather challenging to employ DNS to exam it, but it is definitely a subject that is worth pursuing in the future.

References

Aref, H. & Zawadzki, I. 1991 Linking of vortex rings. *Nature* **354** (6348), 50–53.

Batchelor, G.K. 2000 *An Introduction to Fluid Dynamics*. Cambridge University Press.

Bretherton, F.P. 1970 A note on Hamilton's principle for perfect fluids. *J. Fluid Mech.* **44** (1), 19–31.

Brissaud, A., Frisch, U., Leorat, J., Lesieur, M. & Mazure, A. 1973 Helicity cascades in fully developed isotropic turbulence. *Phys. Fluids (1958–1988)* **16** (8), 1366–1367.

Canuto, C., Hussaini, M.Y., Quarteroni, A. & Zhang, T.J. 2012 *Spectral Methods in Fluid Dynamics*. Springer Science & Business Media.

Cheng, M., Lou, J. & Lim, T.T. 2016 Evolution of an elliptic vortex ring in a viscous fluid. *Phys. Fluids* **28** (3), 037104.

Chichak, K.S., Cantrill, S.J., Pease, A.R., Chiu, S.-H., Cave, G.W.V., Atwood, J.L. & Stoddart, J.F. 2004 Molecular borromean rings. *Science* **304** (5675), 1308–1312.

Dhanak, M.R. & de Bernardinis, B. 1981 The evolution of an elliptic vortex ring. *J. Fluid Mech.* **109**, 189–216.

Hide, R. 1989 Superhelicity, helicity and potential vorticity. *Geophys. Astrophys. Fluid Dyn.* **48** (1–3), 69–79.

Kerr, R.M. 2018*a* Enstrophy and circulation scaling for Navier–Stokes reconnection. *J. Fluid Mech.* **839**, R2.

Kerr, R.M. 2018*b* Trefoil knot timescales for reconnection and helicity. *Fluid Dyn. Res.* **50** (1), 011422.

Kida, S. & Takaoka, M. 1987 Bridging in vortex reconnection. *Phys. Fluids* **30** (10), 2911–2914.

Kida, S. & Takaoka, M. 1988 Reconnection of vortex tubes. *Fluid Dyn. Res.* **3** (1–4), 257–261.

Kida, S. & Takaoka, M. 1994 Vortex reconnection. *Annu. Rev. Fluid Mech.* **26** (1), 169–177.

Kivotides, D. & Leonard, A. 2003 Computational model of vortex reconnection. *Europhys. Lett.* **63** (3), 354.

Kivotides, D. & Leonard, A. 2021 Helicity spectra and topological dynamics of vortex links at high Reynolds numbers. *J. Fluid Mech.* **911**, A25.

Kleckner, D. & Irvine, W.T. 2013 Creation and dynamics of knotted vortices. *Nat. Phys.* **9** (4), 253–258.

Laing, C.E., Ricca, R.L. & Sumners, D.W. 2015 Conservation of writhe helicity under anti-parallel reconnection. *Sci. Rep.* **5**, 9224.

Levy, Y., Degani, D. & Seginer, A. 1990 Graphical visualization of vortical flows by means of helicity. *AIAA J.* **28** (8), 1347–1352.

Martinez, A., Ravnik, M., Lucero, B., Visvanathan, R., Žumer, S. & Smalyukh, I.I. 2014 Mutually tangled colloidal knots and induced defect loops in nematic fields. *Nat. Mater.* **13** (3), 258–263.

McGavin, P. & Pontin, D.I. 2019 Reconnection of vortex tubes with axial flow. *Phys. Rev. Fluids* **4** (2), 024701.

Melander, M.V. & Hussain, F. 1988 Cut-and-connect of two antiparallel vortex tubes. In *Studying Turbulence Using Numerical Simulation Databases*, vol. 2, pp. 257–286. Center for Turbulence Research.

Melander, M.V. & Hussain, F. 1994 Core dynamics on a vortex column. *Fluid Dyn. Res.* **13** (1), 1–37.

Moffatt, H.K. 1969 The degree of knottedness of tangled vortex lines. *J. Fluid Mech.* **35** (1), 117–129.

Moffatt, H.K. & Ricca, R.L. 1992 Helicity and the Călugăreanu invariant. *Proc. R. Soc. Lond.* A **439**, 411–429.

Moreau, J.J. 1961 Constantes d'un îlot tourbillonnaire en fluide parfait barotrope. *C. R. Acad. Sci. Paris* **252**, 2810–2812.

Pohl, W.F. 1968 The self-linking number of a closed space curve. *J. Math. Mech.* **17**, 975–985.

Pradeep, D.S. & Hussain, F. 2004 Effects of boundary condition in numerical simulations of vortex dynamics. *J. Fluid Mech.* **516**, 115–124.

Proment, D. & Krstulovic, G. 2020 Matching theory to characterize sound emission during vortex reconnection in quantum fluids. *Phys. Rev. Fluids* **5** (10), 104701.

Ricca, R.L. & Moffatt, H.K. 1992 The helicity of a knotted vortex filament. In *Topological Aspects of the Dynamics of Fluids and Plasmas*, pp. 225–236. Springer.

Sadlo, F., Hausner, P., Hofmann, L., Jung, P., Karch, G., Peikert, R., Pilz, L., Roth, M. & Sdeo, K. 2019 VCG ParaView plugins.

SAFFMAN, P.G. 1970 The velocity of viscous vortex rings. *Stud. Appl. Maths* **49** (4), 371–380.
SCHEELER, M.W., KLECKNER, D., PROMENT, D., KINDLMANN, G.L. & IRVINE, W.T. 2014 Helicity conservation by flow across scales in reconnecting vortex links and knots. *Proc. Natl Acad. Sci.* **111** (43), 15350–15355.
SCHEELER, M.W., VAN REES, W.M., KEDIA, H., KLECKNER, D. & IRVINE, W.T. 2017 Complete measurement of helicity and its dynamics in vortex tubes. *Science* **357** (6350), 487–491.
WU, J.Z., MA, H.Y. & ZHOU, M.D. 2007 *Vorticity and Vortex Dynamics*. Springer Science & Business Media.
XIONG, S. & YANG, Y. 2019 Construction of knotted vortex tubes with the writhe-dependent helicity. *Phys. Fluids* **31** (4), 047101.
XIONG, S. & YANG, Y. 2020*a* Effects of twist on the evolution of knotted magnetic flux tubes. *J. Fluid Mech.* **895**, A28.
XIONG, S. & YANG, Y. 2020*b* Evolution and helicity analysis of linked vortex tubes in viscous flows. *Sci. Sin. Phys. Mech. Astron.* **50** (4), 040005.
YAO, J. & HUSSAIN, F. 2020*a* On singularity formation via viscous vortex reconnection. *J. Fluid Mech.* **888**, R2.
YAO, J. & HUSSAIN, F. 2020*b* A physical model of turbulence cascade via vortex reconnection sequence and avalanche. *J. Fluid Mech.* **883**, A51.
YAO, J. & HUSSAIN, F. 2020*c* Separation scaling for viscous vortex reconnection. *J. Fluid Mech.* **900**, R4.
YAO, J. & HUSSAIN, F. 2021 Polarized vortex reconnection. *J. Fluid Mech.* **922**, A19.
YAO, J. & HUSSAIN, F. 2022 Vortex reconnection and turbulence cascade. *Annu. Rev. Fluid Mech.* **54**, 317–347.
YAO, J., YANG, Y. & HUSSAIN, F. 2021 Dynamics of a trefoil knotted vortex. *J. Fluid Mech.* **923**, A19.
ZHAO, X. & SCALO, C. 2021 Helicity dynamics in reconnection events of topologically complex vortex flows. *J. Fluid Mech.* **920**, A30.
ZHAO, X., YU, Z., CHAPELIER, J.-B. & SCALO, C. 2021 Direct numerical and large-eddy simulation of trefoil knotted vortices. *J. Fluid Mech.* **910**, A31.
ZUCCHER, S. & RICCA, R.L. 2017 Relaxation of twist helicity in the cascade process of linked quantum vortices. *Phys. Rev.* E **95** (5), 053109.
ZUCCHER, S. & RICCA, R.L. 2019 Momentum of vortex tangles by weighted area information. *Phys. Rev.* E **100** (1), 011101.